Tampere University

Anna Vesala

SURFACE LATTICE RESONANCES FOR MULTIRESONANT SECOND-HARMONIC GENERATION

Faculty of Engineering and Natural Sciences (ENS)
Master of Science (Technology) Thesis
November 2023

In loving memory
of my parents

ABSTRACT

Anna Vesala: Surface Lattice Resonances for Multiresonant Second-Harmonic Generation
Master of Science (Technology) Thesis
Tampere University
Master's Programme in Science and Engineering
Major: Advanced Studies in Engineering Physics
Examiners: Dr. Mikko Huttunen
November 2023

Nonlinear optics plays a critical role in various fields ranging from laser manufacturing to biomedical imaging. However, due to the inherently weak nonlinear response of materials, achieving substantial nonlinear responses often requires long interaction lengths and phase-matching techniques. This presents a significant challenge when attempting to implement nonlinear optics in small volumes. As a result, it is necessary to develop creative and specialized approaches to overcome the constraints imposed by weak nonlinear effects.

One way to address the low nonlinear conversion efficiency in small dimensions is through the use of artificial structures called metamaterials. Plasmonic metamaterials are of particular interest in nanoscale nonlinear optics because they can exhibit collective responses called surface lattice resonances (SLRs), which produce strong local fields that can enhance nonlinear effects. Unfortunately, the conversion efficiencies of plasmonic metamaterials are not yet as high as those of conventional nonlinear materials. To improve the performance of nonlinear optics at the nanoscale, researchers need to explore new metamaterial designs and techniques.

Research on nonlinear plasmonic metamaterials in recent years has mainly centered on materials showcasing a single SLR at either the pump or signal wavelength of a nonlinear process. Our work delves into enhancing the conversion efficiency of second harmonic generation (SHG) through the use of multiresonant metamaterials that are resonant at both the signal and pump wavelengths.

In this Thesis, a thorough investigation is conducted on two metasurfaces that demonstrate multiresonant behavior. These metasurfaces consist of a rectangular arrangement of aluminum nanoparticles on a glass substrate. We first measured angle-resolved optical transmission spectra to show the position and dispersion of the SLRs in our samples. This way, we are able to extract information about the pump wavelengths and incident angles that allow for multiresonant behavior. Next, we measured the variation in second-harmonic emission of the metasurfaces with respect to both pump wavelength and incident angle. By comparing the results obtained under multiresonant and non-multiresonant conditions, we can then understand how multiresonant metasurfaces affect the emission of SHG.

The results presented in this work provide strong evidence for the effectiveness of multiresonant metamaterials in nonlinear optics. Our preliminary linear experiments demonstrated that the SLRs in our samples had an angle-dependent behavior that was in excellent agreement with different modeling methods. Furthermore, the nonlinear experiments illustrated SHG that reached its maximum value when the sample exhibited multiresonant behavior. By tilting the samples, we were able to obtain a roughly 10-fold enhancement of SHG at multiple wavelength-angle combinations. This approach has provided a new way to tailor the properties of metamaterials and could lead to the development of flat, tunable nonlinear devices.

Keywords: nonlinear optics, second-harmonic generation, surface lattice resonance, metasurface.

PREFACE

This Thesis was written as part of the Science and Engineering Master's Programme at Tampere University. The experimental research was conducted in the Nonlinear Optics group together with M.Sc. Timo Stolt. This work was accomplished in collaboration with the University of Eastern Finland. Therefore, I extend my heartfelt appreciation to Dr. Heikki Rekola and Dr. Petri Karvinen for their exceptional work in sample fabrication, and to Prof. Tommi K. Hakala for his supervision throughout the fabrication process. Their expertise and dedication have been vital to our projects success, and I am privileged to have had the opportunity to work with them.

Above all, I wish to express my immense gratitude to my esteemed supervisor, Dr. Mikko Huttunen, for his invaluable guidance, constructive feedback and encouragement over the years. Additionally, I extend my gratitude to Professor Martti Kauranen for providing me with the opportunity to work on exciting topics in the field of nonlinear optics and for his guidance during the early stages of my career. I also wish to express my appreciation to all of my past and present colleagues in the Laboratory of Photonics, including Timo, Antti, Madona, Jussi, Kiia, and Niklas, with whom I have had extensive and insightful discussions. Being part of such a close-knit team has been an incredible experience. Furthermore, I would like to thank Subhajit for taking the time to introduce me to clean rooms and show me how to operate the scanning-electron microscope to capture high-quality images of metamaterials.

Lastly, I would like to express my sincere appreciation to my beloved family, my parents Helena and Risto, my brothers Markus and Lauri, and my sister-in-law Yuexin for their unconditional support and for being my primary source of motivation. My deepest gratitude belongs to my fiancé Joram, who is always by my side, and ready to celebrate even the smallest of victories.

Tampere, 8th November 2023

Anna Vesala

CONTENTS

LIST OF FIGURES

LIST OF SYMBOLS AND ABBREVIATIONS

AL	Achromatic lens
CMOS	Complementary metal–oxide semiconductor
DDA	Discrete-dipole approximation
DFG	Difference-frequency generation
DM	Dichroic mirror
ELA	Empty-lattice approximation
FBZ	First Brillouin zone
FDTD	Finite-difference time-domain
FWM	Four-wave mixing
HWP	Half-wave plate
LP	Linear polarizer
LPF	Long-pass filter
LSA	Lattice-sum approach
LSPR	Localized surface plasmon resonance
MLWA	Modified long-wavelength approximation
Nd:YAG	Neodymium-doped yttrium aluminum garnet
NLST	Nonlinear scattering theory
OPO	Optical parametric oscillator
PMT	Photomultiplier tube
PD	Photodiode
PML	Perfectly-matched layer
Q-factor	Quality-factor
RA	Rayleigh anomaly
SEM	Scanning-electron microscope
SFG	Sum-frequency generation
SHG	Second-harmonic generation
SLR	Surface lattice resonance
SM	Spectrometer
SPDC	Spontaneous parametric down-conversion

SPF	Short-pass filter
Ti:sapph	Titanium sapphire
THG	Third-harmonic generation

$\mathbf{A}$	Interaction matrix
A_{b}	Area of laser beam
α	Polarizability
$\mathbf{a_1}, \mathbf{a_2}, \mathbf{a_3}$	Primitive lattice vectors
$\mathbf{b_1}, \mathbf{b_2}, \mathbf{b_3},$	Primitive reciprocal lattice vectors
$\chi^{(n)}$	n^{th}-order susceptibility tensors
$c.c.$	Complex conjucate of the previous term
$\mathbf{E}$	Electric field
ϵ_0	Dielectric constant
f	Focal length
γ	Damping rate
$\mathbf{G}$	Momentum Vector
$\mathbf{H}$	Magnetic field intensity
I	Intensity
i, j	Diffraction order
$\mathbf{k}$	Wavevector
λ	Wavelength in air
n	Refractive index
N	Number of neighbouring particles
ν_{rep}	Pulse repetition rate
ω	Angular frequency
$\mathbf{p}$	Dipole moment
P	Power
p_x, p_y	Periodicity along x and y-axis
ϕ	Azimuthal angle
$\mathbf{R}$	Lattice vector
S	Surface area
S'	Lattice summation-term
t	Time
τ	Pulse width

T	Transpose of a matrix
θ	Angle of incidence
$\mathbb{Z}$	Set of integers

1 INTRODUCTION

Nonlinear optics is a subfield of modern optics that studies a rich diversity of nonlinear effects associated with the interaction between high-intensity light and matter [1]. In nonlinear processes, light induces a material polarization that depends superlinearly on the strength of the fundamental electric field, leading to exciting effects such as frequency conversion and supercontinuum generation [2]. Achieving such a significant modification from the typical linear optical properties of a material through nonlinear optics generally requires the use of high-power laser light [3]. Consequently, many pioneering works in nonlinear optics occurred in the early 1960s [4–7], following the invention of the first ruby laser [8]. Since its experimental discovery, nonlinear optics has quickly become essential for a wide range of applications, including spectroscopy [9, 10], telecommunications and all-optical data processing [11] and quantum information technologies [12].

With the rise of integrated photonics, there has been a growing demand for nonlinear components that are efficient, miniaturized, and cost-effective [13–15]. Continuous innovations in nanofabrication techniques are addressing this need, facilitating the mass production of compact devices [16, 17]. Despite these technological advancements, the inherent weakness of nonlinear processes presents hurdles in further downsizing nonlinear devices. The attainment of practical conversion efficiencies often requires long interaction lengths and phase-matching techniques [3]. To meet these demands, nonlinear materials of considerable size like bulky photonic crystals or elongated waveguides are employed [1]. Although these materials excel in producing substantial nonlinear signals, especially when situated within optical resonators [18], incorporating them into nanophotonic systems, where the optical near-fields interact with nonlinear media over just a few wavelengths or even at subwavelength scales, poses a significant challenge.

Plasmonic metasurfaces consisting of metallic nanostructures have emerged as a viable option for achieving efficient nanoscale nonlinear optics [19]. When a metasurface containing an array of coupled plasmonic nanoparticles is exposed to light, the resulting interaction can create collective resonances known as surface lattice resonances (SLRs) [20]. These SLRs are of broad scientific interest due to their considerably narrow linewidths, which indicate strong local-field enhancements at the metasurface interface [21]. In the context of nonlinear optics, where light–matter interactions are governed by higher powers of the fields, the potential to increase local fields by utilizing SLRs of metasurfaces is particularly relevant [22, 23]. Despite their enormous potential, the conversion efficiencies of metamaterials still remain lower compared to conventional nonlinear materials. To

enhance the performance of nonlinear optics at the nanoscale, it is crucial for researchers to investigate novel metamaterial designs and methods.

Prior research of plasmonic metamaterials has predominantly focused on exploiting SLRs at either the pump wavelength [24–26] or, in rare cases, the signal wavelength of a nonlinear process [27]. However, to enhance the conversion efficiency of nonlinear plasmonic metamaterials, we propose an alternative approach. Specifically, we propose the utilization of multiresonant metasurfaces, which possess the capability of simultaneously containing SLRs at both the pump and signal wavelengths. By doing so, we aim to amplify the overall nonlinear response of the metamaterial by increasing the intensity of the local fields at two different wavelengths.

This Thesis investigates the impact of multiresonant operation of SLRs on second-harmonic generation (SHG), a second-order nonlinear process. SHG occurs when two photons, possessing the same frequency, combine to produce a single photon with twice the original frequency [4]. The intensity of SHG is sensitive to variations in the local field due to its fourth power dependence on the input field amplitude. Therefore, the use of multiresonant samples is expected to significantly influence this process.

Our research methodology consists of two primary stages. The first stage is devoted to acquiring a thorough understanding of the dispersive properties of our samples. To achieve this, we obtain angle-resolved linear transmission spectra from the metamaterials. This is a crucial step since our samples may not demonstrate multiresonant behavior under normal incidence. Furthermore, we aim to show multiple instances of multiresonant behaviour under different conditions to ensure the reliability and consistency of our research findings. By analyzing the spectra, we can identify the set of angles and wavelengths that facilitate multiresonant behavior. In the second stage, we investigate the impact of multiple SLRs on SHG, utilizing our recently acquired understanding of the conditions that lead to multiresonant behavior. To accomplish this, we will measure angle-resolved SHG emissions from the samples as a function of pump wavelength and analyze the results by examining the differences in the nonlinear response of the samples when the samples exhibit multiresonant behavior and when they do not.

This Thesis consists of five chapters that aim to provide an in-depth understanding of multiresonant metamaterials in the context of nonlinear optics. Chapter 1 serves as an introduction to this Thesis and it discusses the motivation behind the research and the goals that are to be achieved. Chapter 2 presents a comprehensive overview of resonant metasurfaces, with a special focus on SLRs and their associated dispersion. To study the dispersion relation of SLRs, three different modeling tools are employed: the empty-lattice approximation (ELA), the lattice-sum approach (LSA), and the finite-difference time-domain method (FDTD). This Chapter also delves into second-order nonlinear processes and discusses how SLRs can be leveraged to enhance their performance. Chapter 3 describes the angle-resolved linear and nonlinear experimental setups used in the study. This Chapter also provides detailed information on the samples used in the experiments, including their fabrication process. Chapter 4 presents the experimental results

from the linear and nonlinear setups. To conclude the Thesis, Chapter 5 provides a summary of the main findings and implications of the study. It also discusses future research directions that could build on the work presented in this Thesis.

2 THEORETICAL BACKGROUND OF PERIODIC STRUCTURES

In the study of metasurfaces, assuming perfect periodicity and translational invariance is necessary for the formulation of simplistic models. While these assumptions aid our analysis and predictions, it's important to note that actual metasurfaces comprise a large, finite number of nanoparticles arranged in a regular pattern. This Chapter opens by introducing the mathematical tools that are essential for describing the structure of lattices. This foundational knowledge sets the stage for a more detailed exploration of metasurfaces and the resonances they exhibit. In the section dedicated to SLRs, we offer an in-depth explanation of determining their spectral location and dispersion, utilizing ELA, LSA, and FDTD methods. As this Chapter progresses, the focus shifts to nonlinear optics, specifically how the dispersive properties of SLRs can be leveraged to induce multiresonant behavior in metamaterials, thereby potentially enhancing nonlinear responses.

2.1 Bravais and Reciprocal Lattice

A Bravais lattice or direct lattice is a collection of regularly spaced points in 3D-space whose positions are determined by multiples of three primitive lattice vectors $\mathbf{a}_1$, $\mathbf{a}_2$, and $\mathbf{a}_3$ [28]. In mathematical terms, we can express the position vector $\mathbf{R}$ of any point in the lattice as

$$\mathbf{R} = o\mathbf{a}_1 + p\mathbf{a}_2 + q\mathbf{a}_3, \qquad o, p, q \in \mathbb{Z} \tag{2.1}$$

where $\mathbb{Z}$ is the set of integers. A simplified 2D-Bravais lattice is illustrated in Figure 2.1(a).

The fundamental building block of the Bravais lattice is the primitive unit cell, which is a region of space that can be translated through all the vectors of the lattice without overlapping or leaving gaps. A primitive unit cell is designed to hold only one lattice point, but if there is more than one lattice point, the unit cell is considered non-primitive. A commonly used primitive unit cell is the Wigner–Seitz cell, which includes all of the space closer to a particular lattice point than to any other point in the lattice. The shaded-in areas in Figure 2.1 mark the Wigner–Seitz cells for each lattice.

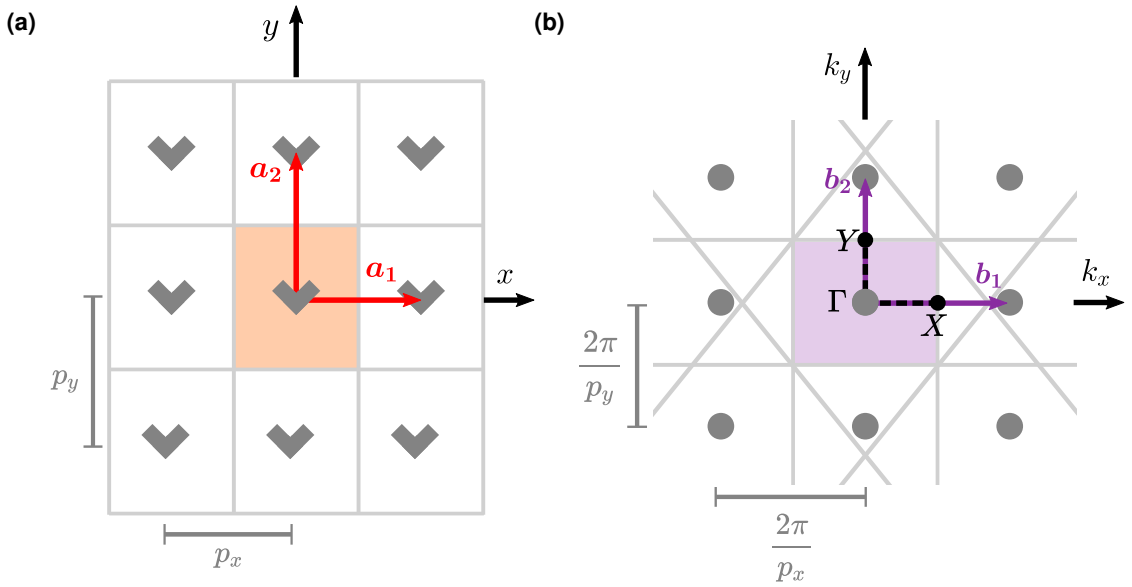

Figure 2.1. Schematic representation of (a) a two-dimensional rectangular Bravais lattice with primitive lattice vectors $\mathbf{a}_1$ and $\mathbf{a}_2$ and the (b) reciprocal lattice with primitive reciprocal lattice vectors $\mathbf{b}_1$ and $\mathbf{b}_2$. The shaded areas in both lattices depict the Wigner–Seitz cells for each space. In the reciprocal lattice, the Wigner–Seitz cell is shown with various points of symmetry marked (Γ, X, Y).

When we perform a Fourier transform of the Bravais lattice, we generate a reciprocal lattice. This reciprocal lattice exists in the spatial frequency space referred to as $\mathbf{k}$-space, where $\mathbf{k}$ represents the wavevector. Figure 2.1(b) illustrates this transformation for a rectangular Bravais lattice. Any point in the reciprocal lattice can be expressed with the momentum vector $\mathbf{G}$ defined by

$$\mathbf{G} = i\mathbf{b}_1 + j\mathbf{b}_2 + k\mathbf{b}_3, \qquad i, j, k \in \mathbb{Z} \tag{2.2}$$

where the vectors $\mathbf{b}_1$, $\mathbf{b}_2$ and $\mathbf{b}_3$ represent the primitive reciprocal lattice vectors. The primitive reciprocal lattice vectors can be constructed based on the primitive Bravais lattice vectors by

$$\mathbf{b}_1 = 2\pi \frac{\mathbf{a}_2 \times \mathbf{a}_3}{\mathbf{a}_1 \cdot (\mathbf{a}_2 \times \mathbf{a}_3)}, \tag{2.3}$$

$$\mathbf{b}_2 = 2\pi \frac{\mathbf{a}_3 \times \mathbf{a}_1}{\mathbf{a}_1 \cdot (\mathbf{a}_2 \times \mathbf{a}_3)}, \tag{2.4}$$

$$\mathbf{b}_3 = 2\pi \frac{\mathbf{a}_1 \times \mathbf{a}_2}{\mathbf{a}_1 \cdot (\mathbf{a}_2 \times \mathbf{a}_3)}. \tag{2.5}$$

From this, one can deduce the simple yet helpful property

$$\mathbf{a}_l \cdot \mathbf{b}_m = 2\pi\delta_{lm}. \tag{2.6}$$

Here, the Kronecker's delta, denoted by δ_{lm}, takes a value of 1 when $l = m$, and a value of 0 for all other cases. This result is derived from two different simplifications. First, the cross product of two vectors produces another vector perpendicular to both original

vectors. Thus, for $l \neq m$, the dot product between this resultant vector and one of the original vectors is zero. On the other hand, when $l = m$, the cyclic nature of the scalar triple product, depicted by the equation $\mathbf{a}_1 \cdot (\mathbf{a}_2 \times \mathbf{a}_3) = \mathbf{a}_2 \cdot (\mathbf{a}_3 \times \mathbf{a}_1) = \mathbf{a}_3 \cdot (\mathbf{a}_1 \times \mathbf{a}_2)$, allows us to simplify the dot product in Equation 2.6 directly to 2π.

The reciprocal lattice is a powerful tool used to study diffraction from an ordered structure such as a periodical metasurface. It offers an accurate and straightforward way to describe most structural properties by taking advantage of the material's periodicity. For instance, researchers typically focus on the First Brillouin Zone (FBZ), which is the Wigner–Seitz cell in the reciprocal lattice closest to the origin ($\mathbf{k}$=$\mathbf{0}$), instead of analyzing the entire reciprocal space [29]. The reason for this is that any value of $\mathbf{k}$ that lies outside the FBZ has a corresponding value within the FBZ that differs by the momentum vector $\mathbf{G}$. As a result, many structural properties of the system can be understood by studying only the FBZ [28].

2.2 Resonant Metasurfaces

Metamaterials are a unique class of artificial materials that demonstrate physical properties not commonly found in naturally occurring materials. In the field of optics, they are engineered to control and manipulate light by arranging subwavelength structures, such as metallic nanoantennas or dielectric nanopillars, in a carefully designed configuration. Despite the complexity of their design, metamaterials behave as homogeneous materials with effective material properties due to the subwavelength size of the individual building blocks. The effective properties of the metamaterials are determined not only by the composition of the constituent materials but also by the shapes and arrangements of the subwavelength structures. By controlling the design parameters, metamaterials can exhibit remarkable responses to light, such as optical magnetism, nanoscale phase engineering, and negative refractive index [30–32].

Plasmonic metasurfaces, composed of metallic nanostructures arranged on a flat surface, have been gaining a significant amount of attention in the field of nonlinear optics in recent years [19, 24]. This interest is driven by the fact that metals possess intrinsic nonlinear optical constants that are significantly larger than those of dielectric materials [3]. Moreover, metal nanoparticles exhibit collective oscillations of conduction electrons, resulting in strong local electromagnetic fields around the nanoparticles. This inherently enhances the interaction between light and matter, thereby offering an alternative for phase-matching schemes in nonlinear experiments. Although losses are significant in plasmonic structures, the far-field coupling among the metallic structures offers a strategic avenue to harness robust and compelling responses [20].

In the sections that follow, we will examine in detail two different resonant modes inherent to plasmonic metasurfaces. These resonant modes, visually depicted in the transmission spectrum shown in Figure 2.2, assume a central role in shaping how light engages with the metasurface structure. Our discussion will predominantly center around the LSPR,

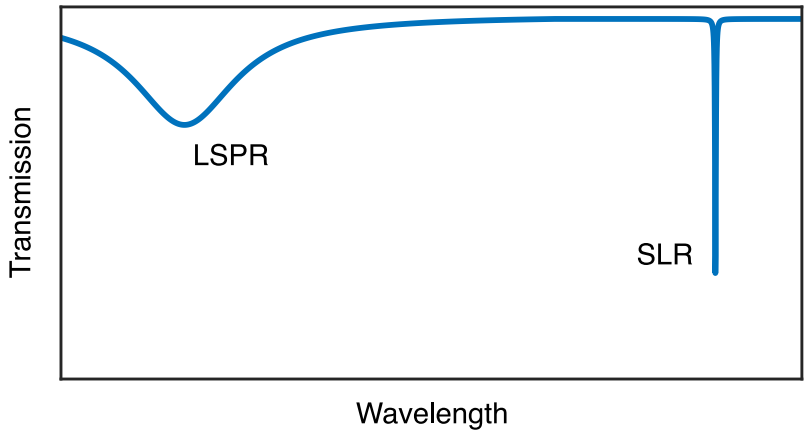

Figure 2.2. A typical transmission spectrum for a plasmonic metasurface exhibiting a localized surface plasmon resonance (LSPR) and surface lattice resonance (SLR).

which pertains to the response of a single nanoparticle, and the SLR, which signifies the collective response of a periodic array of metal nanoparticles. A thorough understanding of these resonances and their properties is essential to fully realize the potential of plasmonic metasurfaces in various applications.

2.2.1 Localized Surface Plasmon Resonance

Metals possess unique optical properties that arise from the movement of their conduction electrons. The movement of conduction electrons inside a metal is conventionally described using the free electron model, which postulates that valence electrons of metals travel without restriction in relation to the stationary, positively charged lattice ions [28]. This freedom of movement enables the formation of a plasmon when metals interact with an electric field. A plasmon is known as a quantum of collective free electron oscillation with respect to the fixed positive ions in a bulk metal. To illustrate this concept further, consider a solid metal object exposed to an external electric field that points downward. The electrons will move upward, exposing positive ions at the bottom, until they neutralize the field within the metal. When the electric field is removed, the electrons begin to move back down, attracted to the unaccompanied positive ions due to long-range Coulomb forces. However, instead of returning directly to their original positions, the electrons continue to oscillate with respect to the positive-ion background at a specific frequency, known as the plasmon frequency. The oscillation of the electrons continues until the energy is gradually lost through factors like resistance or damping. The plasmon frequency, governing this oscillation, is determined by two essential factors: the concentration of free electrons present in the metal and the effective mass of an electron.

Metal nanoparticles also have the capacity to host plasmons. Within these nanoparticles, conduction electrons oscillate collectively in relation to their heavier ionic core. Owing to the nanoparticle's limited dimensions, the plasmons are confined to the surfaces of the nanoparticle. When an oscillating electric field is applied, precisely matching the resonant

frequency of the plasmon, it results in a highly coherent oscillation of the charge density creating an oscillating dipolar mode, as shown in Figure 2.3. This, in turn, induces a secondary electric near field around the structure and causes a substantial amplification of the electric field in the vicinity of the nanoparticle [33]. Such specialized behavior is classified as an LSPR. The confinement of irradiated light into subwavelength scales has led to diverse practical applications of LSPRs, including the development of biosensors [34], plasmon-enhanced photocatalysis [35] and nonlinear optics [27]. It is important to note that the LSPR is produced at a distinct resonant wavelength and is not spatially dispersive [36]. Moreover, for an LSPR to occur, the wavelength of the incident electric field should be significantly larger than the dimensions of the metal nanoparticle, ensuring that the dipole approximation holds and the electrons experience a relatively uniform electric field simultaneously.

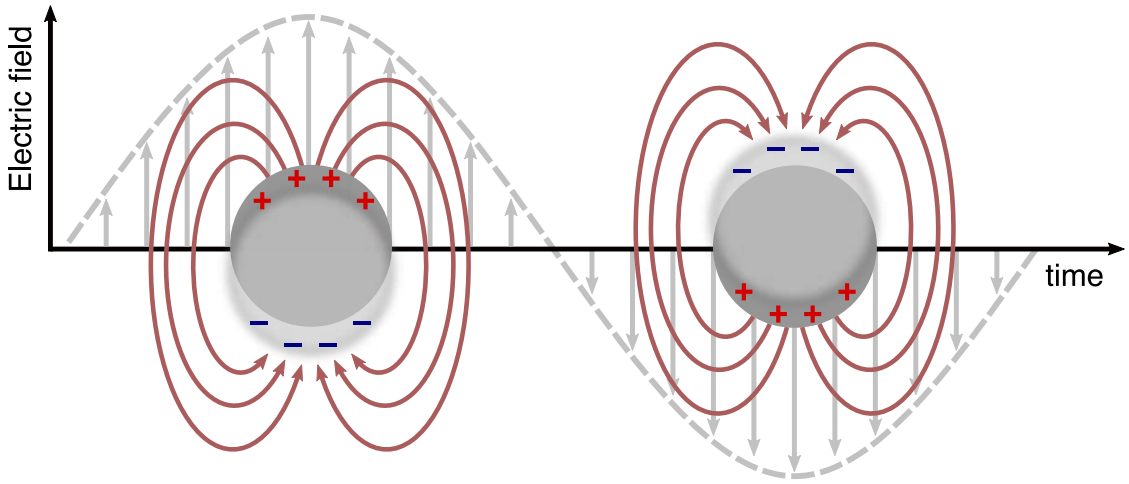

Figure 2.3. The temporal behavior of an LSPR, revealing the oscillation of charge density and the resulting induced electric near field.

When designing metasurfaces for various applications, it is crucial to have control over the spectral location of the LSPR. Fortunately, there are several well-established qualitative factors that influence the spectral location. One such factor is the plasmon length, which represents the distance over which the oscillations occur. Interestingly, while nanoparticles can vary in shape, those constructed from the same material will present similar LSPR spectra if their plasmon lengths are comparable [37]. The easiest way to modify the plasmon length is by adjusting the size of nanoparticles [38]. The size of a particle directly influences the oscillations, with larger particles causing the oscillations to span a greater distance, consequently leading to a redshift in the wavelength of the LSPR. The polarization of incident light can also influence the plasmon length, although this relationship may not be immediately apparent. When the induced dipoles align with the polarization direction of the incident light, the consequent electric current flows along a path inside the nanoparticle, connecting the opposite charges of the induced dipole. The path length of this current flow may vary for different polarizations, as demonstrated by the black arrows in Figure 2.4, particularly in the case of V-shaped nanoparticles. In V-shaped nanoparticles aligned with their symmetry axis parallel to the y-axis, x-polarized light has

a longer LSPR wavelength than y-polarized light. This is because y-polarized light induces oscillations along the arms, while x-polarized light causes oscillations across the entire V-shaped structure. In addition to plasmon length, the composition of the nanostructure and the refractive index of the surrounding medium are significant determinants of the LSPR's spectral location [39, 40].

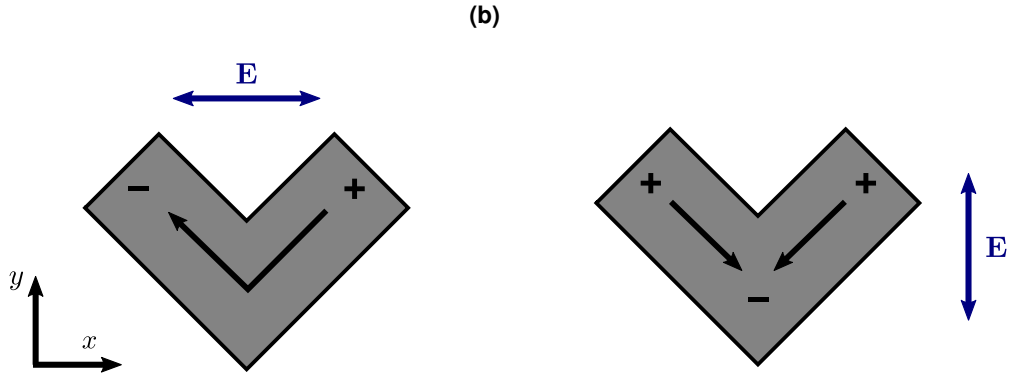

Figure 2.4. The charge distribution caused by an LSPR in a V-shaped metal nanoparticle for (a) x-polarized and (b) y-polarized incident light. The resonance wavelength is redshifted for x-polarized light compared to y-polarized light because the x-polarized incident light couples with plasmons that are associated with a longer effective length.

Although LSPRs have advantages, their strong radiative damping typically leads to weak resonances with a low-quality factor (Q-factor) of approximately 10, thereby restricting their potential applications [20]. The Q-factor provides a measure of the oscillator's ability to sustain oscillations without significant decay over time and it is determined by the ratio of the resonance wavelength λ_{res} to the width of the resonance $\Delta\lambda$. Unfortunately, the Q-factor of the LSPR is largely independent of the geometry of the nanostructure, and little can be done to improve the sharpness of the plasmon resonance once the material and resonance frequency are determined [41].

2.2.2 Surface Lattice Resonances

Fortunately, and at first sight rather surprisingly, the optical properties of nanoparticles can be significantly influenced by the presence of other plasmonic materials in close proximity. Through a strategic arrangement of nanostructures, it is possible to surpass the limitations associated with weak LSPRs. This enhanced performance arises from the way nanoparticles, when organized into a periodic array, behave much like a diffraction grating. At a particular incident angle or wavelength, the diffracted waves can move parallel to the surface of the grating. If the metallic nanoparticles are organized into an array with a spacing that matches the wavelength of a single particle resonance then the diffractive modes of the array and the LSPRs can couple creating a collective resonance called SLR. In contrast to the confined nature of LSPRs, these collective modes predominantly propagate outside the metallic nanoparticles. Furthermore, SLRs display other

unique characteristics, including spatial dispersion and notably high Q-factors, reaching a peak value of 2340 [21].

One important property of SLRs is their strong dependence on polarization, which greatly affects the extent of radiative coupling in different lattice directions. This dependence arises from the nonuniform dipolar radiation pattern typically exhibited by LSPRs in a homogeneous environment. To elaborate, when a nanoparticle is illuminated by an electric field with a polarization that aligns parallel to the metasurface plane, the nanoparticle exhibits characteristics of an electric dipole emitting radiation primarily confined within the metasurface plane but propagating orthogonally to the polarization direction [42]. This leads to effective coupling between nanoparticles orthogonal to the polarization, resulting in the formation of in-plane perpendicular SLRs. While diagonal coupling can also occur, it is worth highlighting that in dielectric media SLRs do not propagate in a direction along the metasurface that is parallel to the polarization.

Figure 2.5 illustrates the coupling directions of nanoparticles with grating diffraction orders denoted by i and j. In this context, it is established that the diffraction order i corresponds to the direction along the x-axis, while the diffraction order j corresponds to the direction along the y-axis. Therefore, if we consider a periodic metasurface that is illuminated with y-polarized incident light, an in-plane y-polarized SLR forms as a result of the interparticle coupling along the x-axis. This particular SLR is denoted as $\text{SLR}_{(i,0)}$. Similarly, when the incident light is x-polarized, an in-plane x-polarized SLR, denoted as $\text{SLR}_{(0,j)}$, arises and propagates along the y-axis. Moreover, by employing either or a combination of both of these polarizations, it is possible to create an SLR that propagates diagonally when both i and j are nonzero. This diagonal SLR is denoted as $\text{SLR}_{(i,j)}$.

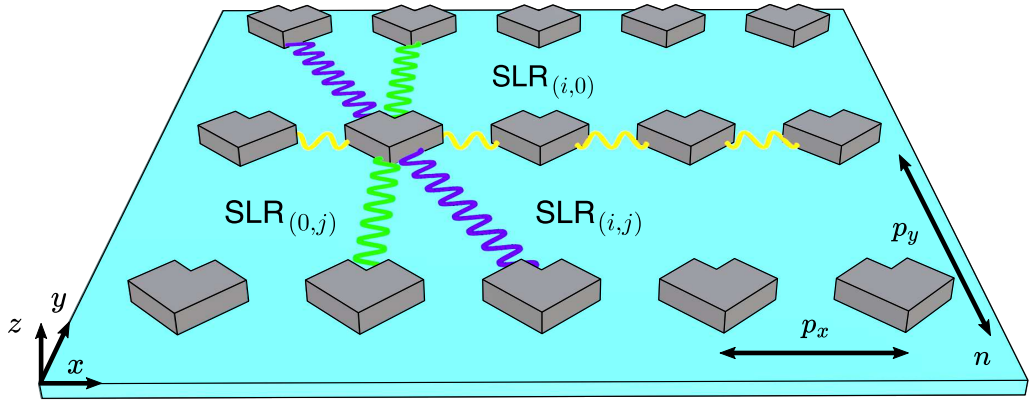

Figure 2.5. The dipolar radiative couplings between metallic nanoparticles possess a polarization dependency, meaning that the coupling usually takes place in a direction that is perpendicular to the polarization that is responsible for generating in-plane SLRs. Therefore, with y-polarized incident light, perpendicular SLRs moving along the x-axis (yellow waves). For x-polarized light, the SLRs propagate along the y-axis (green waves). Diagonal SLRs (blue waves) can be produced with both polarizations.

It's worth noting that at higher energy levels, metallic nanoparticles can also exhibit high-order modes such as quadrupoles or octopoles. In these instances, the previously mentioned argument no longer applies as the higher-order modes possess different radiative patterns as compared to the typical dipolar distribution [43, 44]. Another significant point to highlight is that the dipolar radiation pattern can be changed in an asymmetrical environment, which in turn can lead to increased coupling capabilities in various directions [45]. Consequently, to study in-plane perpendicular and diagonal SLRs, we need to study nanoparticles in a homogeneous environment.

2.3 Methods for Determining Surface Lattice Resonance Dispersions

To thoroughly understand the characteristics of waves traveling through periodic structures, energy–momentum or equivalently wavelength–wavevector dispersion relations need to be studied. Within this section, we introduce three different methods for determining the dispersion curves, including one theoretical, one analytical, and one numerical approach. By familiarizing oneself with various models and comparing them, the advantages and disadvantages of each method can be evaluated, and an understanding of when to apply each method most effectively can be gained.

2.3.1 Empty-Lattice Approximation

The ELA is the most simple theoretical model of photonic lattices where the dispersion characteristics of the lattice are computed in the limit of vanishing nanoparticle volume. While crude, it is still a powerful tool when studying the modes of the lattice. In the ELA framework, a grating-related effect called the Rayleigh anomaly (RA) is utilized to comprehend the behaviour of SLRs. The RA describes the phenomenon wherein a metasurface supports the propagation of a diffracted wave along its diffraction grating. Such propagation is contingent on the conservation of in-plane momentum, which can be expressed as

$$\mathbf{k}_{\mathrm{sub}} = \mathbf{k}_{\mathrm{inc}} + \mathbf{G}, \tag{2.7}$$

where $\mathbf{k}_{\mathrm{inc}}$ is the tangential wavevector component of the incident wave (i.e. parallel to the metasurface), $\mathbf{k}_{\mathrm{sub}}$ is the wavevector of the diffracted wave propagating along the metasurface and $\mathbf{G}$ is the momentum vector previously defined in Chapter 2.1. Because the SLR can be interpreted as a form of Fano interaction between the discrete RA and the broad LSPR [46], we can estimate the spectral position of in-plane SLRs using the location of RAs. However, it's worth noting that while SLRs usually appear close to RA wavelengths, they don't precisely coincide. Such discrepancies arise from phase shifts introduced by resonant nanoparticles, a detail the ELA neglects.

As a special case, we apply Equation 2.7 to a light–matter interaction between a linearly polarized incident wave and a metasurface with a transparent dielectric surrounding,

where n_{sup} and n_{sub} are the refractive indexes for the superstate and substrate materials, respectively. Using the above conservation of momentum on the component form of the substrate wavevector provides

$$\|\mathbf{k}_{\mathrm{sub}}\|^2 = \|\mathbf{k}_{\mathrm{sub,x}}\|^2 + \|\mathbf{k}_{\mathrm{sub,y}}\|^2 = (\|\mathbf{k}_{\mathrm{inc,x}}\| + i\|\mathbf{b}_1\|)^2 + (\|\mathbf{k}_{\mathrm{inc,y}}\| + j\|\mathbf{b}_2\|)^2. \tag{2.8}$$

If we assume that the incoming light of wavelength λ impinges the metasurface at an incident angle θ_{sup}, we can take the tangential component of the wavevector to be of the form $k_{\mathrm{inc}} = \frac{2\pi}{\lambda} n_{\mathrm{sup}} \sin\theta_{\mathrm{sup}}$. Because our experiments take place in air, we can simplify the incident wavevector expression by using Snells law and simply write that $k_{\mathrm{inc}} = \frac{2\pi}{\lambda}\sin\theta$, where θ is now the angle of incidence in air. For nanoparticles arranged into a rectangular lattice, Equation 2.8 then turns into

$$\left(\frac{2\pi n}{\lambda_{(i,j)}}\right)^2 = \left(\frac{2\pi}{\lambda_{(i,j)}}\sin\theta\cos\phi + i\frac{2\pi}{p_x}\right)^2 + \left(\frac{2\pi}{\lambda_{(i,j)}}\sin\theta\sin\phi + j\frac{2\pi}{p_y}\right)^2, \tag{2.9}$$

where $\lambda_{(i,j)}$ is the spectral wavelength of an SLR, i and j are the same diffraction orders discussed in Chapter 2.2.2, ϕ is the azimuthal angle that defines the incident plane, n is the refractive index of the substrate, and p_x and p_y are the lattice constants for the metasurface. By canceling out the common factors and rearranging Equation 2.9, we end up with a quadratic function of the form

$$\lambda_{(i,j)}^2\left(\frac{i^2}{p_x^2} + \frac{j^2}{p_y^2}\right) + \lambda_{(i,j)} 2\sin\theta\left(\cos\phi\frac{i}{p_x} + \sin\phi\frac{j}{p_y}\right) + \sin^2\theta - n^2 = 0. \tag{2.10}$$

This has a solution that is given by

$$\lambda_{(i,j)} = -A + \sqrt{A^2 - B}, \tag{2.11}$$

if we choose A and B such that

$$A = \frac{\sin\theta}{(i/p_x)^2 + (j/p_y)^2}\left(\cos\phi\frac{i}{p_x} + \sin\phi\frac{j}{p_y}\right) \tag{2.12}$$

and

$$B = \frac{\sin^2\theta - n^2}{(i/p_x)^2 + (j/p_y)^2}. \tag{2.13}$$

Admittedly, the ELA does not address the linear polarization of light. Instead, it displays all the possible resonances that can occur within the lattice. However, by taking into account the type of SLR formed, a more comprehensive understanding of the dependence of resonances on polarization and lattice geometry can be gained. Therefore, we proceed with our analysis while limiting our examination to in-plane perpendicular SLRs, which were briefly discussed in Chapter 2.2.2.

To investigate in-plane perpendicular SLRs, we will examine two linear polarizations of light. We begin by using ELA to analyze x-polarized light impinging on our sample in the

yz-incident plane. In this scenario, the azimuthal angle is $\phi = \frac{\pi}{2}$, and the polar angle is $\theta = \theta_y$. Therefore, A and B become

$$A = \frac{\sin\theta_y}{(i/p_x)^2 + (j/p_y)^2}\left(\frac{j}{p_y}\right) \tag{2.14}$$

and

$$B = \frac{\sin^2\theta_y - n^2}{(i/p_x)^2 + (j/p_y)^2}. \tag{2.15}$$

Under the given conditions, the perpendicular SLR that emerges is x-polarized and propagates in the y-direction with a diffraction order of $i = 0$ and $j = j$. Consequently, the formulations for A and B are reduced to

$$A = \frac{\sin\theta_y}{j}p_y \tag{2.16}$$

and

$$B = \frac{\sin^2\theta_y - n^2}{j^2}p_y^2. \tag{2.17}$$

With this simplification, we can rewrite the spectral wavelength of the x-polarized SLR$_{(0,j)}$ as

$$\lambda_{(0,j)} = -\frac{\sin\theta_y}{y}p_y + \sqrt{\frac{n^2p_y^2}{j^2}} = p_y\left(\frac{n}{|j|} - \frac{\sin\theta_y}{j}\right). \tag{2.18}$$

On the contrary, when light polarized in the y-direction hits the sample along the xz-plane, the azimuthal and polar angles are defined as $\phi = 0$ and $\theta = \theta_x$. In this case, a y-polarized perpendicular SLR emerges that travels along the x-axis with a diffraction order of $i = i$ and $j = 0$. By following a method similar to the one used for x-polarized incident light, we can express the spectral wavelength of the y-polarized SLR$_{(i,0)}$ as

$$\lambda_{(i,0)} = -\frac{\sin\theta_x}{i}p_x + \sqrt{\frac{n^2p_x^2}{i^2}} = p_x\left(\frac{n}{|i|} - \frac{\sin\theta_x}{i}\right). \tag{2.19}$$

For a rectangular lattice, Equations 2.18 and 2.19 suggest that the spectral position of an in-plane perpendicular SLR is influenced by the spacing in the direction orthogonal to the incident polarization. Additionally, the spectral position of an SLR is influenced by both the diffraction order and the angle of incidence. Notably, the sign of the diffraction orders becomes crucial when light strikes the sample at an oblique angle, given that diffraction orders can be either positive or negative. At a normal incidence, two SLRs will overlap if their i and j diffraction orders have the same absolute values, respectively. This will manifest in a dispersion diagram as a singular, pronounced SLR peak, despite it representing two diffraction orders. However, upon tilting the sample, these modes diverge, with the dispersion diagram presenting an SLR peak that distinctively splits into two peaks at oblique angles of incidence. The observed splitting and shifting of an SLR occurs exclusively when the rotation is performed about the in-plane axis that is perpendicular to the direction of the SLR propagation. This relationship allows for easy post-fabrication

tuning of the wavelength of in-plane SLRs, as schematically depicted in Figure 2.6. Such simple and sensitive tuning would not be achievable with single-particle responses such as LSPRs.

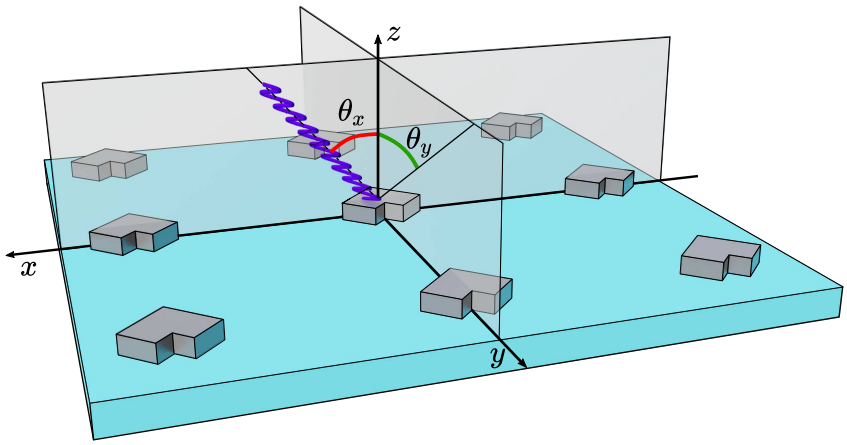

Figure 2.6. By tilting the sample along a specific plane, it is possible to modify the spectral location of perpendicular SLRs. When tilting the sample about the y-axis (altering θ_x), the wavelength of an SLR$_{(i,0)}$ that is y-polarized can be adjusted. Similarly, tilting the sample about the x-axis (altering θ_y) allows for tuning of the wavelength of an SLR$_{(0,j)}$ that is x-polarized. Diagonal SLRs can be adjusted by a tilt in either direction.

Metasurfaces exhibit not only in-plane perpendicular SLRs but also in-plane diagonal SLRs. Light polarized in the x- or y-direction can stimulate these diagonal SLRs, which arise due to coupling along the lattice diagonals. Regardless of the linear incident polarization, the diagonal SLRs appear at the same wavelength when the metasurface is illuminated at normal incidence. This wavelength is given by

$$\lambda_d = n\frac{p_x p_y}{p_d}. \tag{2.20}$$

Here, $p_d = \sqrt{p_x^2 + p_y^2}$ represents the diagonal length of the unit cell of the metasurface.

The diagram in Figure 2.7 illustrates the ELA solutions, as light interacts with a metasurface with a rectangular lattice at different angles of incidence, θ. The lattice's periodicities were set to p_x = 398 nm and p_y = 813 nm, and the substrate was chosen to be a dielectric with a refractive index of n = 1.51. The dispersion of the metasurface is shown along the high-symmetry directions of the FBZ by altering the angle of incidence either in the xz-plane (θ_x) or the yz-plane (θ_y). The dashed black lines and labeled high-symmetry points in the reciprocal space illustrated in Figure 2.1(a) show the path taken in this dispersion relation. A total of four SLRs are visible at the Γ-point in the selected wavelength range and the diffraction orders for these SLRs are listed in ascending order of energy: (i,j) = $(0, \pm 1)$, $(0, \pm 2)$, $(\pm 1, 0)$, and $(\pm 1, \pm 1)$. The computations for the complete dispersion relation only took a few seconds, indicating that ELA is a computationally efficient

method.

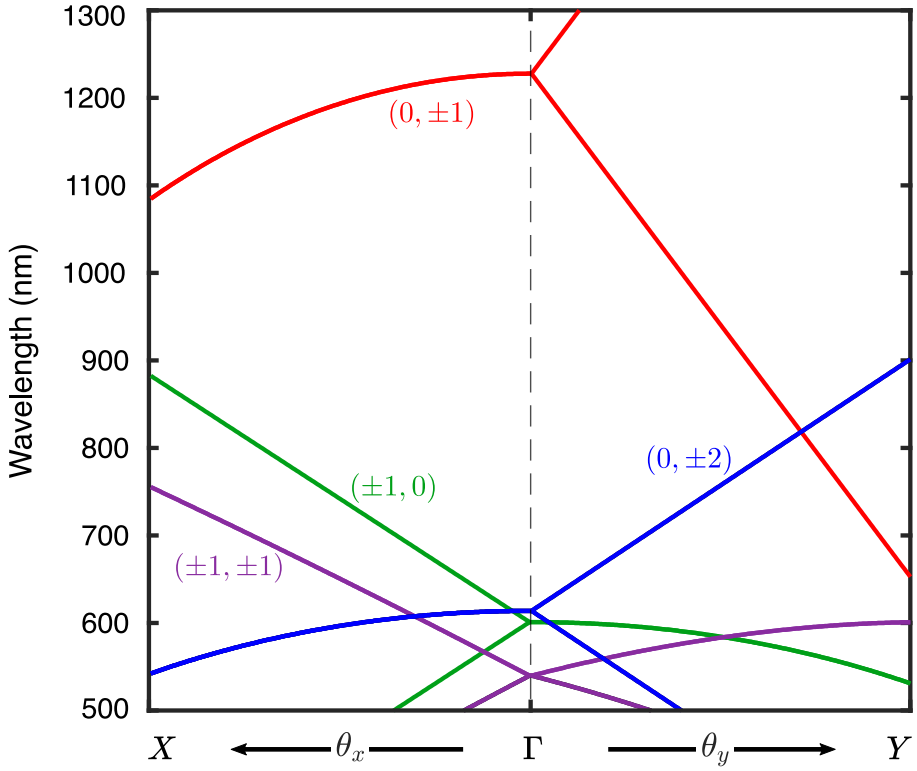

Figure 2.7. Dispersion of a metasurface as determined by the ELA. The metasurface is composed of nanoparticles that are considered to be negligible in size on a dielectric substrate and they are organized into a rectangular lattice with a periodicity of p_x = 398 nm and p_y = 813 nm. The angle of incidence is separately adjusted in the xz-plane (θ_x) and the yz-plane (θ_y) to reveal the dispersion along the high-symmetry directions of the FBZ. The various diffraction orders are distinctly indicated by solid lines of different colors.

The influence of polarization on different SLRs can be readily observed by examining the dispersion relation obtained by the ELA. The two SLRs with the lowest energy, specifically the x-polarized SLR$_{(0,\pm1)}$ and SLR$_{(0,\pm2)}$, exhibit a splitting and a significant change in their spectral position when the sample is tilted about the x-axis and the angle θ_y is modified. On the other hand, the most energetic diagonal SLR$_{(\pm1,\pm1)}$ splits and shifts its spectral position when the sample is tilted about both the x-axis and the y-axis. Lastly, the SLR$_{(\pm1,0)}$, which is polarized in the y-direction and is positioned between the x-polarized and diagonal SLRs, experiences a dramatic alteration in its spectral location and a splitting when the sample is tilted about the y-axis with an angle θ_x.

2.3.2 Lattice-Sum Approach

The LSA is an effective method for semi-analytically modeling electrostatic interactions in periodic systems. It uses point dipoles to represent nanoparticles and evaluates the combined impact of an incident plane wave and scattered electric fields from neighboring dipoles on a single dipole in the array. This information is then used to calculate the effective polarizability, which reflects the nanoparticles' tendency to acquire an electric dipole

moment when exposed to electric fields from various sources. The LSA method closely resembles the discrete-dipole approximation (DDA) [47, 48], but it simplifies calculations by assuming that all nanoparticles have the same dipole moment ($\mathbf{p}_c = \mathbf{p}$ for all c). This is valid only when an array contains identical dipoles whose response closely mimics that of nanoparticles located at only the center of the array. This assumption is not unfounded as it has been proven to be quite accurate through a comparison of LSA with DDA and FDTD simulations [49, 50].

To derive the necessary equations for the LSA, we begin by examining the total local electric field at the position of the c^{th} particle, represented by $\mathbf{E}_c$. The total local field is a sum of the incident field $\mathbf{E}_{\text{inc},c}$ and the scattered electric field from N nearby polarizable nanoparticles which can be expressed as

$$\mathbf{E}_c = \mathbf{E}_{\text{inc},c} - \sum_{d=1}^{N} \mathbf{A}_{cd}\mathbf{p}_d. \tag{2.21}$$

Here, $\mathbf{p}_d$ is the dipole moment of the neighboring d^{th} dipole. The inclusion of a negative sign before the summation is a matter of convention and does not affect the overall interpretation. The term $\mathbf{A}_{cd}$ is an interaction matrix that depicts the optical coupling strength between the d^{th} and the c^{th} particle. It is determined by evaluating the following expression

$$\mathbf{A}_{cd} = \frac{\mathrm{e}^{\mathrm{i}kr_{cd}}}{\epsilon_0 r_{cd}} \left[k^2(\hat{\mathbf{r}}_{cd}\hat{\mathbf{r}}_{cd}^{\mathsf{T}} - \mathbf{I}_3) - \frac{1 - \mathrm{i}kr_{cd}}{r_{cd}^2}(3\hat{\mathbf{r}}_{cd}\hat{\mathbf{r}}_{cd}^{\mathsf{T}} - \mathbf{I}_3) \right], \quad c \neq d \tag{2.22}$$

where r_{cd} is the distance between the coordinates $\mathbf{r}_c$ and $\mathbf{r}_d$, and $\hat{\mathbf{r}}_{cd}$ denotes the unit vector that points from $\mathbf{r}_c$ to $\mathbf{r}_d$. The matrix $\mathbf{I}_3$ represents a 3×3 identity matrix and the transpose of a matrix is denoted by writing the symbol $^{\mathsf{T}}$ in superscript on the right side of the matrix in question.

Next, we wish to express the right side of Equation 2.21 in terms of the dipole moment of the c^{th} particle in order to identify the terms that contribute to the effective polarizability of a particle. By applying the Bloch theorem, we can describe the relationship between dipole moments in a periodic array using the equation

$$\mathbf{p}_d = \mathrm{e}^{\mathrm{i}\mathbf{k}\cdot\mathbf{R}_{dc}}\mathbf{p}_c, \tag{2.23}$$

where $\mathbf{k}$ is the wave vector of the incident field, and $\mathbf{R}_{dc}$ is the lattice vector between the d^{th} and the c^{th} particle. Additionally, we can express the incident field near the c^{th} particle in terms of its dipole moment, by using

$$\mathbf{E}_{\text{inc},c} = (\epsilon_0\alpha_c)^{-1}\,\mathbf{p}_c, \tag{2.24}$$

where ϵ_0 is the vacuum permittivity, and α_c is the polarizability of the c^{th} particle. Assuming that the polarizability remains constant or static over time, the LSA remains valid for particles with a size parameter approximately 100 times smaller than the incident wave-

length or less. However, if we desire to study larger particles that are more relevant to plasmonic experiments while still using the simple dipole approximation, we need to use the modified long-wavelength approximation (MLWA). The MLWA takes into account two important factors that become increasingly significant with an increase in particle size: radiative damping due to spontaneous emission and dynamic depolarization due to retardation [51]. The polarizability using MLWA is expressed as follows

$$\alpha_c(\omega) = \frac{\alpha_{\text{static}}(\omega)}{1 - \frac{2}{3}\mathrm{i}k^3\alpha_{\text{static}}(\omega) - \frac{k^2}{l}\alpha_{\text{static}}(\omega)} \tag{2.25}$$

where l describes the effective length of the particle. The term $\alpha_{\text{static}}(\omega)$ is a static polarizability of a small lorentzian scatterer and is written as

$$\alpha_{\text{static}}(\omega) = \frac{A_0}{\omega_{\text{res}} - \omega - \mathrm{i}\gamma}. \tag{2.26}$$

In the equation, A_0 represents the resonance strength constant, ω denotes the angular frequency, ω_{res} is the resonant frequency, and γ corresponds to the damping rate. These different parameters can be obtained experimentally, for example, by fitting curves to numerical simulations.

Now by substituting Equation 2.23 and Equation 2.24 into Equation 2.21 and making the assumption that all dipole moments, or equivalently polarizabilities, of all nanoparticles are identical, we finally arrive at the following expression

$$\mathbf{E}_c = \left((\epsilon_0\alpha)^{-1} - \sum_{d=1}^{N} \mathbf{A}_{cd}\mathrm{e}^{\mathrm{i}\mathbf{k}\cdot\mathbf{R}_{dc}}\right)\mathbf{p}_c \equiv \left((\epsilon_0\alpha)^{-1} - S'\right)\mathbf{p}_c, \tag{2.27}$$

where S' refers to the redefined lattice-summation term. From this formulation, it becomes straightforward to identify the effective particle polarizability as

$$\alpha^* = \frac{1}{\alpha^{-1} - \epsilon_0 S'}. \tag{2.28}$$

Upon closer examination, we observe that when the real components of α^{-1} and $\epsilon_0 S'$ are equal, the denominator in Equation 2.28 approaches zero, resulting in the polarizability tending towards infinity. This condition signifies the excitation of an SLR. In the case where the oscillations of the SLRs occur within the plane of the metasurface, we can simplify the expression for S' as

$$S' = \sum_{d=1}^{N} \mathrm{e}^{\mathrm{i}\mathbf{k}\cdot\mathbf{R}_{dc}} \frac{\mathrm{e}^{\mathrm{i}kr_{cd}}}{\epsilon_0 r_{cd}} \left[k^2 \sin^2\phi_d + \frac{(1 - \mathrm{i}kr_{cd})(3\cos^2\phi_d - 1)}{r_{cd}^2}\right] \tag{2.29}$$

where ϕ_d is the angle between r_{cd} and the dipole moment p_c.

Once the effective polarizability is established, the final step entails visualizing the dispersion of the supported SLR modes, which becomes apparent through an angle-resolved transmission spectrum. To acquire this spectrum, we evaluate the extinction cross-

section based on the values obtained from the LSA according to [52]

$$\sigma^*_{\text{ext}} = 4\pi k N \text{Im}(\alpha^*). \tag{2.30}$$

From the perspective of SLRs and their Q-factors, it is evident from this equation that the depth of a resonance is directly proportional to the magnitude of the imaginary component of the effective polarization, specifically $\text{Im}\left((\alpha^{-1} - \epsilon_0 S')^{-1}\right)$.

We employed the LSA to compute the angle-resolved extinction spectra of a metasurface illuminated with x-polarized incident light. The metasurface design, with lattice periodicities of p_x = 398 nm and p_y = 813 nm, and a substrate refractive index of n = 1.51, was consistent with the configuration used in the ELA. The calculations specifically focused on the visible and near-infrared regions, which had been previously identified as susceptible to SLRs according to the conclusions from the ELA analysis. Typically, the lattice sums in LSA are computed for infinite lattices ($N \to \infty$), and various techniques are available for conducting such calculations [53]. However, in our specific calculations, a finite number of particles were considered, precisely 62,500 particles arranged in a 200 $\times$ 100 μm^2 array. With these parameters, each transmission spectrum in our simulations required a few seconds to compute. Consequently, the execution time for this process was slightly longer compared to the ELA analysis.

Figure 2.8 illustrates the dispersion relation obtained from the LSA analysis, revealing distinctive SLRs characterized by abrupt dips in transmission. Notably, only three SLRs can be observed at normal incidence, which have the diffraction orders: (i,j) = $(0, \pm 1)$, $(0, \pm 2)$, and $(\pm 1, \pm 1)$. The absence of the y-polarized SLR corresponding to the diffraction order $(\pm 1, 0)$ can be attributed to the polarization considerations of LSA and our deliberate use of exclusively x-polarized light during the calculations. This result once again showcases the significant influence of incident polarization on the behavior of SLRs.

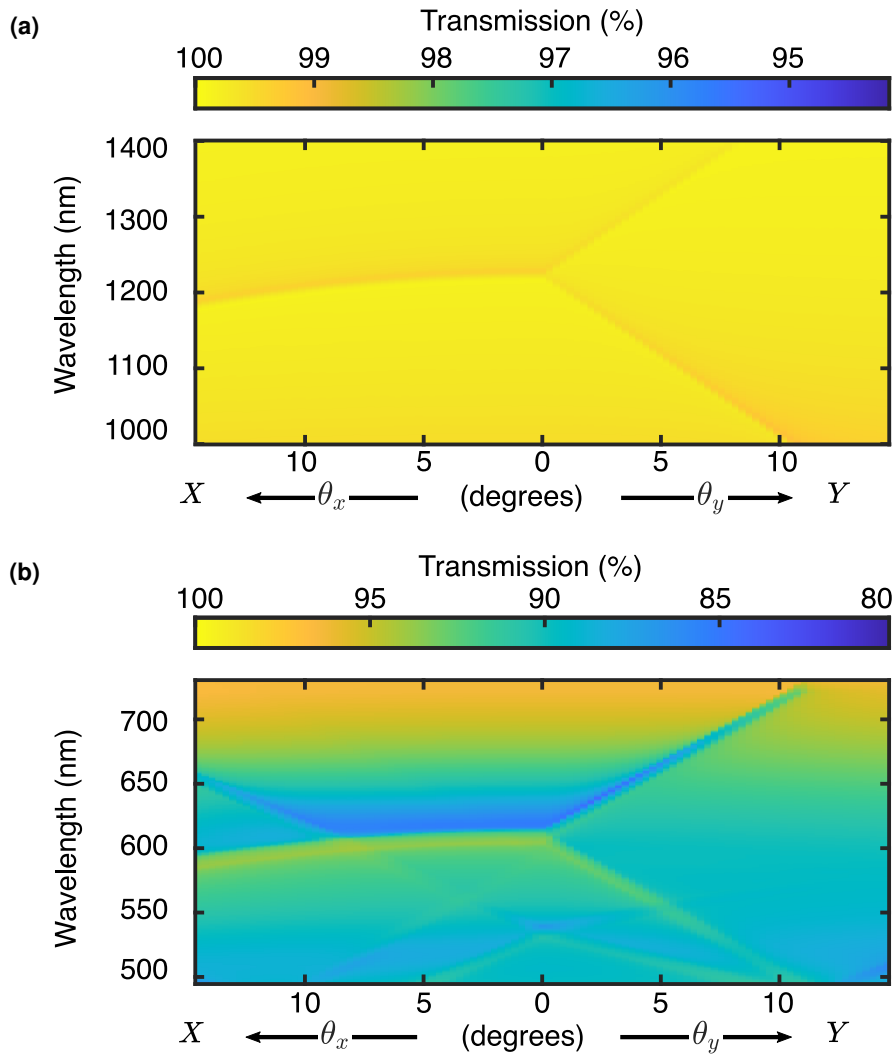

Figure 2.8. Dispersion diagram obtained from the LSA in the (a) near-infrared and (b) visible wavelengths with x-polarized incident light. The contour plot illustrates the relationship between transmission, incident angle, and incident wavelength for a metasurface made up of point dipole scatterers organized in a lattice with a periodicity of p_x = 398 nm and p_y = 813 nm. The angle of incidence is altered in the xz-plane (θ_x) and the yz-plane (θ_y).

Overall, when comparing the results obtained from the LSA and the ELA, there is a relatively good agreement regarding the dispersive behavior of the three SLRs that existed in both methods. The slight difference in resonance peak locations can be attributed to the LSA's consideration of coherent phase accumulation among neighboring particles. However, these variations remain minimal, with the maximum observed redshift for the same SLR at normal incidence reaching only 7 nm.

2.3.3 Finite-Difference Time-Domain Method

When dealing with nanoparticles of more intricate shapes, there are no analytical or theoretical solutions available. Therefore, it is necessary to use numerical methods to rigorously solve electromagnetic interactions. To accomplish this, a 3D FDTD solver

was utilized as the final tool for modeling dispersion relations. The FDTD method is a numerical technique that approximates the partial derivatives in Maxwell's equations as differences between adjacent points in space or time, allowing the solution of the differential equations to be reduced to a set of finite-difference equations, which can be efficiently computed [54]. The FDTD is especially well-suited for examining metamaterials across a wide frequency range since it operates in the time domain and requires only one simulation to determine the spectral response for all frequencies and the field evolution around the nanoparticle.

In this Thesis, we employed the Ansys Lumerical FDTD 2021 R2.4 software to numerically compute the dispersion relation of V-shaped aluminum nanoparticles. Similar to other techniques, these nanoparticles were placed within a homogeneous medium characterized by a refractive index of 1.51, while being arranged in a rectangular lattice with periodicities of p_x = 398 nm and p_y = 813 nm. Each unit cell consisted of a single nanoparticle with specific dimensions of arm length = 100 nm, arm width = 70 nm, and thickness = 30 nm. The symmetry axis of the nanoparticles was aligned along the y-axis, as depicted in Figure 2.5.

To accurately simulate the behavior of the entire periodic metasurface, a white plane-wave light source was utilized to illuminate a single unit cell. Periodic boundary conditions were employed in the in-plane dimensions (x- and y-axes), while perfectly-matched layers (PMLs) were utilized in the out-of-plane dimension (z-axis). In order to capture the transmitted power across a wide wavelength range (400 nm–1300 nm), domain power monitors were employed. To account for the changes in the angle of incidence, we optimized the PML design to minimize reflections at oblique angles. Additionally, when the incident angle deviated from normal incidence, we employed a broadband fixed angle source technique (BFAST) in the simulations to incorporate the incident angle's influence on the wavelength. For calculations, a non-uniform mesh was employed, featuring a finer mesh specifically around the nanoparticle to improve accuracy. Within this region, the mesh size peaked at 3 nm.

The dispersion relation obtained numerically with the FDTD method is depicted in Figure 2.9. Given the lengthy simulation time of approximately 24 hours per transmission spectrum, we had to carefully choose the input polarization and plane of incidence. To successfully accomplish the objectives of this Thesis with the generation of type-I SHG, it is crucial to design a sample that allows for independent control of two SLRs with orthogonal polarizations. Therefore, we utilized two different input polarizations in the FDTD simulations, but not across all wavelengths. We only needed to utilize x-polarized incident light in the near-infrared wavelength range to excite the x-polarized $\text{SLR}_{(0,\pm1)}$. For the visible wavelength range, we only employed y-polarized light to induce the y-polarized $\text{SLR}_{(\pm1,0)}$ and $\text{SLR}_{(\pm1,\pm1)}$.

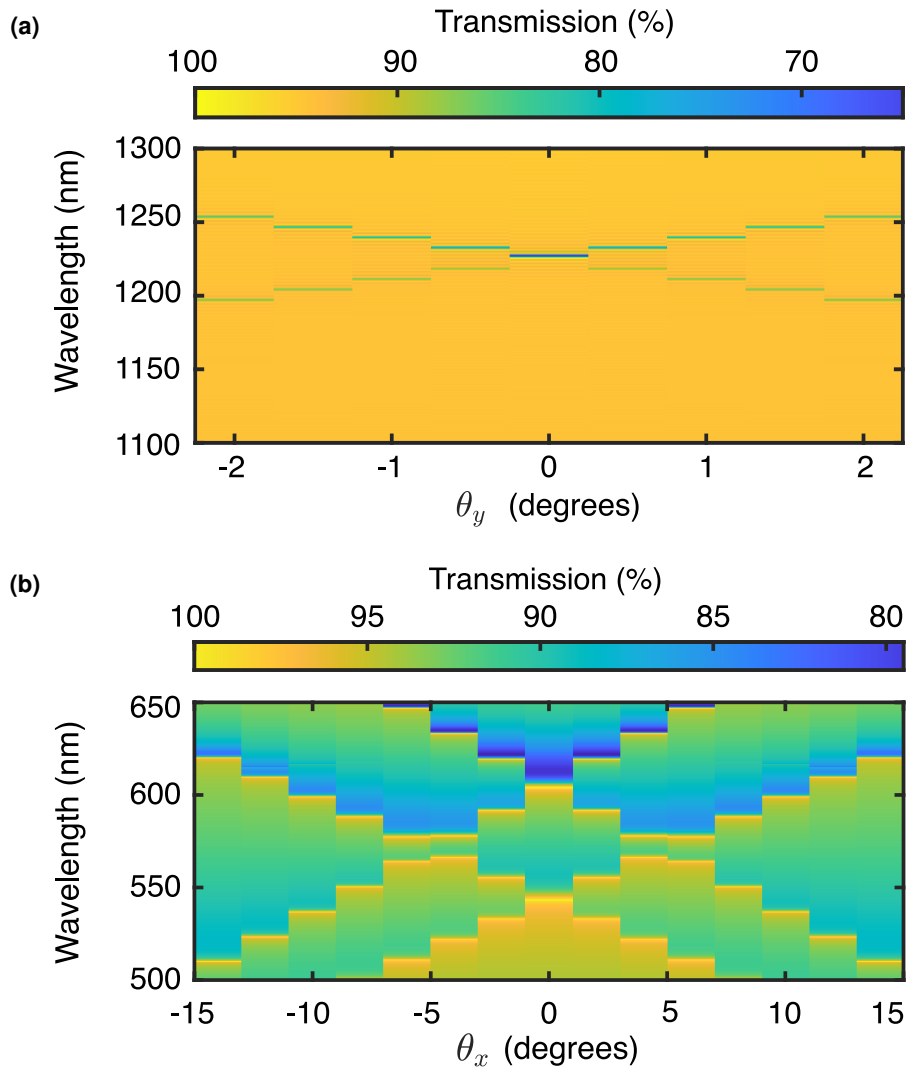

Figure 2.9. Dispersion diagram obtained with FDTD that displays transmission as a function of incident angle and wavelength for a metasurface being illuminated with (a) x and (b) y-input polarization in different spectral regions. The metasurface is composed of aluminum V-shaped nanoparticles that are arranged in a lattice with a period of p_x = 398 nm and p_y = 813 nm. With y-polarized light, the angle of incidence is only adjusted in the xz-plane (θ_x), and for x-polarized light, the angle of incidence is adjusted only in the yz-plane (θ_y).

In selecting the plane of incidence for the simulated dispersion diagram, we specifically focused on the plane that exhibited the greatest spatial dispersion, as predicted by the relationships discussed in Chapter 2.3.1. In Equation 2.18, we observed that the wavelength of $\text{SLR}_{(0,\pm1)}$ is solely dependent on θ_y. Therefore, we tilted the sample around the x-axis to thoroughly investigate the behavior of the SLR at near-infrared wavelengths. Similarly, according to Equation 2.19, the spectral location of $\text{SLR}_{(\pm1,0)}$ is determined solely by θ_x, leading us to tilt the sample about the y-axis for visible wavelengths. While the diagonal resonance $\text{SLR}_{(\pm1,\pm1)}$ in Figure 2.9(b) should exhibit sensitivity to tilting both about the x-axis and y-axis regardless of the polarization used, our simulations only demonstrated its dispersive behavior with tilts about the y-axis using y-polarized light.

The FDTD simulations demonstrate a high degree of alignment with the ELA, with only a minimal discrepancy of approximately 3 nm in the spectral locations of SLRs. While FDTD offers a high level of precision, the significant duration required for each transmission spectrum simulation can make it challenging to analyze trends and characteristics of entire metasurfaces during the design process.

2.4 Nonlinear Optics

Having examined the capabilities of SLRs, we shall now delve into the fundamental principles of nonlinear optics and investigate the potential applications of SLRs in this area. To begin, we will examine the effects of a weak electric field on a medium. As is well-known, the interaction of light with a medium induces electric dipoles within the material. The cumulative effect of these induced dipole moments produces a time-varying electrical polarization field $\mathbf{P}(t)$. This field is usually linearly proportional to the incident electric field $\mathbf{E}\left(t'\right)$ and can be represented in the most general case by the integral

$$\mathbf{P}(t) = \epsilon_0 \int_{-\infty}^{\infty} \chi^{(1)}\left(t - t'\right) \cdot \mathbf{E}\left(t'\right) \mathrm{d}t' \tag{2.31}$$

where ϵ_0 is the dielectric constant, and $\chi^{(1)}\left(t - t'\right)$ is the linear susceptibility tensor that possesses a rank of two. The equation represents the polarization of the medium at a given time, t, as a result of the electric field at all previous points in time $t - t'$. The polarization is expressed through the response function $\chi^{(1)}\left(t - t'\right)$, which encapsulates all information regarding the material's properties. It is important to note that $\chi^{(1)}\left(t - t'\right)$ must be zero for $t' \geq t$ to ensure causality is maintained. This equation can be interpreted as the convolution integral between the electric field and the linear susceptibility tensor. In this particular context, our focus is specifically on the time domain, due to the utilization of the electric dipole approximation, which remains applicable in the case of nanoparticles. Given that the wavelengths employed are notably greater than the atomic length scale, we can fairly assume that the electric fields and susceptibilities do not exhibit dependence on spatial quantities such as $\mathbf{r}$ and $\mathbf{k}$.

The transformation of Equation 2.31 into the frequency domain can be facilitated by utilizing the definitions of the Fourier transform and its inverse with relevant variables. We can define the Fourier transform over time and its inverse over angular frequency ω as follows

$$\mathcal{F}\{f(t)\} = f(\omega) = \int_{-\infty}^{\infty} f(t) \mathrm{e}^{\mathrm{i}\omega t} \mathrm{d}t, \tag{2.32}$$

and

$$\mathcal{F}^{-1}\{f(\omega)\} = f(t) = \frac{1}{2\pi} \int_{-\infty}^{\infty} f(\omega) \mathrm{e}^{-\mathrm{i}\omega t} \mathrm{d}\omega. \tag{2.33}$$

When we express the time-dependent variables $\chi^{(1)}\left(t - t'\right)$ and $\mathbf{P}(t)$ in Equation 2.31 in terms of their representations as inverse Fourier transforms over the frequency domain,

as specified by Equation 2.33, we obtain with some rearranging

$$\frac{1}{2\pi}\int_{-\infty}^{\infty}\mathbf{P}(\omega)\mathrm{e}^{-\mathrm{i}\omega t}\mathrm{d}\omega=\epsilon_0\int_{-\infty}^{\infty}\frac{1}{2\pi}\chi^{(1)}\left(\omega\right)\mathrm{e}^{-\mathrm{i}\omega t}\left(\int_{-\infty}^{\infty}\mathbf{E}\left(t'\right)\mathrm{e}^{\mathrm{i}\omega t'}\mathrm{d}t'\right)\mathrm{d}\omega. \tag{2.34}$$

The expression enclosed in brackets can be recognized as the Fourier transform of the time-varying electric field, which can be equivalently written as $\mathbf{E}\left(\omega\right)$. With some simplification, we end up with

$$\int_{-\infty}^{\infty}\mathbf{P}(\omega)\mathrm{d}\omega=\epsilon_0\int_{-\infty}^{\infty}\chi^{(1)}\left(\omega\right)\cdot\mathbf{E}\left(\omega\right)\mathrm{d}\omega. \tag{2.35}$$

Recognizing that this equality must hold for every frequency leads us to the frequency domain description of a linear response

$$\mathbf{P}(\omega)=\epsilon_0\chi^{(1)}\left(\omega\right)\cdot\mathbf{E}\left(\omega\right). \tag{2.36}$$

Examining the similarities between the electric field and induced polarization in the frequency domain reveals that the material's polarization follows oscillations that match the frequency of the incident field. This description, however, accurately represents the material's behavior only when the incident fields have relatively low intensity. As the intensity of the incoming light surpasses a certain threshold, the material's response becomes more complex and nonlinearity comes into play. In most cases, the nonlinear expression for $\mathbf{P}(t)$, can be approximated as a power series of $\mathbf{E}(t)$, so that

$$\begin{aligned}\mathbf{P}(t)=&\epsilon_0\int_{-\infty}^{\infty}\chi^{(1)}\left(t-t_1\right)\cdot\mathbf{E}\left(t_1\right)\mathrm{d}t_1.\\&+\epsilon_0\int_{-\infty}^{\infty}\chi^{(2)}\left(t-t_1;t-t_2\right):\mathbf{E}\left(t_1\right)\mathbf{E}\left(t_2\right)\mathrm{d}t_1\,\mathrm{d}t_2\\&+\epsilon_0\int_{-\infty}^{\infty}\chi^{(3)}\left(t-t_1;t-t_2;t-t_3\right)\vdots\mathbf{E}\left(t_1\right)\mathbf{E}\left(t_2\right)\mathbf{E}\left(t_3\right)\mathrm{d}t_1\,\mathrm{d}t_2\,\mathrm{d}t_3+\cdots,\end{aligned} \tag{2.37}$$

where $\chi^{(n)}$ represents the susceptibility tensor of the n^{th} order, possessing a rank of (n + 1) and encompassing $3^{(n+1)}$ components. In order for the material's response to be physically meaningful within this approximation, the power series expansion must converge. Nevertheless, there are situations where this series fails to converge, a situation known as a non-perturbative process [3]. While these situations may require different methods to understand nonlinear optical effects, the power series treatment is adequate for the scope of this study.

Given that any electric field $\mathbf{E}\left(t\right)$ can be represented as a combination of monochromatic plane waves, we have

$$\mathbf{E}\left(t\right)=\sum_i\mathbf{E}\left(\omega_i\right). \tag{2.38}$$

From this, we can simplify the Fourier transform of Equation 2.37 to

$$\mathbf{P}(\omega)=\mathbf{P}^{(1)}(\omega)+\mathbf{P}^{(2)}(\omega)+\mathbf{P}^{(3)}(\omega)+\cdots, \tag{2.39}$$

where the nonlinear polarization is given by

$$\mathbf{P}^{(n)}(\omega) = \epsilon_o \chi^{(n)} \left(\omega = \sum_i \omega_i \right) \prod_i \mathbf{E}\left(\omega_i\right). \tag{2.40}$$

Our research focuses specifically on second-order nonlinear effects $\left(\mathbf{P}^{(2)}\right)$. These effects are widely utilized in traditional nonlinear applications due to their notable strength compared to other higher-order nonlinear processes. While the other nonlinear effects are worth investigating, we have chosen to leave their exploration for future research endeavors.

2.4.1 Second-Order Nonlinear Processes

Second-order nonlinearity gives rise to the lowest-order nonlinear processes and it is fundamental to a range of optical processes, including optical frequency conversion. To understand the different types of second-order processes, we will begin by considering two intense monochromatic plane waves of frequencies ω_1 and ω_2 interacting with a nonlinear medium. The resultant electric field is described by

$$\mathbf{E}(t) = \mathbf{E}_1 \mathrm{e}^{-\mathrm{i}\omega_1 t} + \mathbf{E}_2 \mathrm{e}^{-\mathrm{i}\omega_2 t} + c.c. = \mathbf{E}\left(\omega_1\right) + \mathbf{E}\left(\omega_2\right) + c.c. \ . \tag{2.41}$$

Here $c.c.$ represents the complex conjugate of the previous terms. To simplify the analysis, we make the assumption that the medium instantaneously reacts to the incident fields. As a result, rather than evaluating a convolution integral, the second-order nonlinear polarization can be expressed as

$$\mathbf{P}^{(2)}(t) = \epsilon_0 \chi^{(2)} \mathbf{E}^2(t). \tag{2.42}$$

By substituting the equation for the electric field as defined in Equation 2.41, we obtain the following alternate expression for the second-order nonlinear polarization

$$\begin{aligned} \mathbf{P}^{(2)}(t) = & \epsilon_0 \chi^{(2)} \Big[\mathbf{E}_1^2 \mathrm{e}^{-2\mathrm{i}\omega_1 t} + \mathbf{E}_2^2 \mathrm{e}^{-2\mathrm{i}\omega_2 t} + 2\mathbf{E}_1 \mathbf{E}_2 \mathrm{e}^{-\mathrm{i}(\omega_1+\omega_2)t} \\ & + 2\mathbf{E}_1 \mathbf{E}_2^* \mathrm{e}^{-\mathrm{i}(\omega_1-\omega_2)t} + c.c. \Big] + 2\epsilon_0 \chi^{(2)} \left[\mathbf{E}_1 \mathbf{E}_1^* + \mathbf{E}_2 \mathbf{E}_2^* \right]. \end{aligned} \tag{2.43}$$

Utilizing a more convenient notation, we can express this as

$$\mathbf{P}^{(2)}(t) = \sum_n \mathbf{P}\left(\omega_n\right) \mathrm{e}^{-\mathrm{i}\omega_n t}, \tag{2.44}$$

where the summation encompasses frequencies ω_n that cover both positive and negative values. Here, the explicit form for all of the complex amplitudes $\mathbf{P}\left(\omega_n\right)$ corresponding to

the different frequency components are

$$\mathbf{P}^{(2)}(2\omega_1) = \epsilon_0 \chi^{(2)}(2\omega_1; \omega_1, \omega_1)\, \mathbf{E}_1^2, \tag{2.45}$$

$$\mathbf{P}^{(2)}(2\omega_2) = \epsilon_0 \chi^{(2)}(2\omega_2; \omega_2, \omega_2)\, \mathbf{E}_2^2, \tag{2.46}$$

$$\mathbf{P}^{(2)}(\omega_1 + \omega_2) = 2\epsilon_0 \chi^{(2)}(\omega_1 + \omega_2; \omega_1, \omega_2)\, \mathbf{E}_1 \mathbf{E}_2, \tag{2.47}$$

$$\mathbf{P}^{(2)}(\omega_1 - \omega_2) = 2\epsilon_0 \chi^{(2)}(\omega_1 - \omega_2; \omega_1, -\omega_2)\, \mathbf{E}_1 \mathbf{E}_2^*, \tag{2.48}$$

$$\mathbf{P}^{(2)}(0) = 2\epsilon_0 \left(\chi^{(2)}(0; \omega_1, -\omega_1)\, \mathbf{E}_1 \mathbf{E}_1^* + \chi^{(2)}(0; \omega_2, -\omega_2)\, \mathbf{E}_2 \mathbf{E}_2^* \right). \tag{2.49}$$

In these equations, we establish a connection between the electric field frequency components and complex conjugates, such that $\mathbf{E}^*(\omega) = \mathbf{E}(-\omega)$. Consequently, we are able to disregard the negative frequency equivalents of Equations 2.45–2.48, as they merely represent the complex conjugates of the original expressions [3].

Each expression in Equations 2.45–2.49 describes a different second-order nonlinear process. The last term, $\mathbf{P}^{(2)}(0)$, is associated with optical rectification, which creates a static electric field within the medium. The remaining polarization components described in Equations 2.45–2.48 are associated with the phenomenon of three-wave frequency mixing. In this process, new frequency components are generated through the combination of the sum and difference of the involved frequencies as summarized in Figure 2.10. In the subsequent discussion, each three-wave frequency mixing process will be thoroughly explored.

The terms $\mathbf{P}^{(2)}(2\omega_1)$ and $\mathbf{P}^{(2)}(2\omega_2)$ represent second harmonic generation (SHG) at frequencies $2\omega_1$ and $2\omega_2$, respectively. During the process of SHG, two photons of frequency ω_1 interact with the nonlinear medium, leading to the excitation of the system to a new state that incorporates the combined energy of the incoming photons, as illustrated in Figure 2.10(a). In second-order processes, the energy of photons does not match any actual electronic states of the material. This results in the temporary nature of the excited state, known as a virtual state, which is indicated by the dashed line in the energy level diagrams. When the system relaxes to the ground state, depicted by a solid line, it emits a coherent photon with twice the frequency of the incident photons. This form of frequency doubling is used for practical applications, such as efficiently shifting the output frequency of a laser. A notable example is the conversion of near-infrared output (at 1064 nm) from a Nd:YAG laser to the visible spectrum (at 532 nm) [55]. This process is particularly significant in the medical field, where a frequency-doubled Nd:YAG laser is commonly used to restore visual clarity following cataract surgery [56].

The term $\mathbf{P}^{(2)}(\omega_1 + \omega_2)$ corresponds to a more general version of SHG called sum-frequency generation (SFG). The SFG process, illustrated in Figure 2.10(b), operates similarly to SHG with the difference of having two incident photons with distinct frequencies, ω_1 and ω_2. Hence, the generated photon has a frequency of $\omega_1 + \omega_2$. A common application of SFG is to generate ultraviolet light by combining the 1064 nm output from an Nd:YAG laser with its frequency-doubled light at 532 nm, producing 355 nm UV light [57]. This UV light has various practical uses, including laser processing of materials,

particularly those that are fragile and hard [58].

Lastly, we consider the term $\mathbf{P}^{(2)}(\omega_1 - \omega_2)$, which corresponds to the process of difference-frequency generation (DFG). The DFG process, depicted in Figure 2.10(c), involves the interaction of two incident photons with frequencies, ω_1 and ω_2. The higher-frequency photon, ω_1, induces excitation of the system into a virtual state from where the system relaxes to a lower virtual state through a stimulated emission at frequency ω_2. During the relaxation of the system, a photon with a frequency equal to the difference between the two incident photons, $\omega_1 - \omega_2$, is emitted. Thus, DFG results in both the generation of a new frequency and gain at the lower of the input frequencies. Techniques utilizing DFG find widespread use in optical parametric oscillators (OPOs), where it is employed to convert the output of a laser source to various frequency ranges, especially near and mid-infrared ranges. Additionally, DFG is used in optical parametric amplification, where the lower frequency photon is amplified [3].

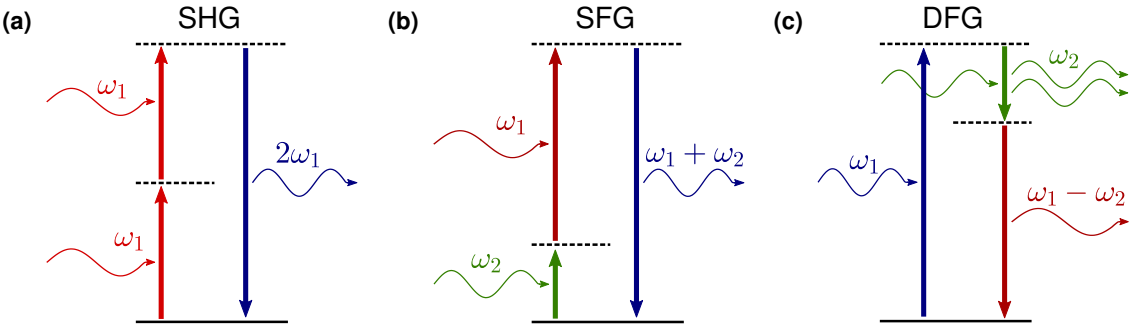

Figure 2.10. Energy level diagrams for (a) SHG, (b) SFG and (c) DFG. The ground states are drawn with solid lines and virtual states with dashed lines. The excitation of the system is shown by upward arrows, while the relaxation is depicted by downward arrows.

In theory, in a lossless and dispersionless material, all second-order nonlinear processes should be comparable in strength. However, due to the intrinsic low efficiencies of these processes, phase-matching techniques are generally employed to enhance them to a practical level. This approach, however, allows for the strengthening of only one frequency component at a time to levels that can be detected. Consequently, it becomes unfeasible to simultaneously observe multiple nonlinear effects within bulk media [3]. In contrast, nonlinear metasurfaces offer a unique advantage. Their subwavelength scale allows for the relaxation of these stringent phase-matching requirements, thereby enabling a wider range of frequency components to be generated while still maintaining a robust signal strength [59].

2.4.2 Engineering Second-Harmonic Responses from Metasurfaces

In order for a material, including metasurfaces, to exhibit a second-order nonlinear response, certain symmetry constraints must be satisfied. In particular, if a material pos-

sesses centrosymmetry, the second-order nonlinear polarization will be zero. This arises from the fact that in a centrosymmetric structure, applying a field of $-\mathbf{E}$ leads to the nonlinear polarization vector following $-\mathbf{P}^{(2)} = \epsilon_0\chi^{(2)}[-\mathbf{E}]^2$ due to spatial inversion. When comparing this to Equation 2.42, we find that $\mathbf{P}^{(2)} = -\mathbf{P}^{(2)}$, which implies that $\chi^{(2)}$ has to be zero. This result is of great significance because it explicitly prevents centrosymmetric materials from displaying second-order nonlinear responses, irrespective of the applied field's intensity. For this reason, traditional second-order nonlinear crystals, like potassium dihydrogen phosphate or barium borate, pertain to crystal point groups characterized by broken inversion symmetry. To break the symmetry in metasurfaces, plasmonic nanostructures that possess broken inversion symmetry, such as V-shaped nanoparticles, can be used.

Once suitable symmetry constraints are met, a strong nonlinear response can be obtained by enhancing the light–matter interaction. According to the nonlinear scattering theory (NLST), the second-harmonic responses of metamaterials are influenced by the local fields, which oscillate at the fundamental frequency $E_{\mathrm{loc}}(\omega)$ and the second-harmonic frequency $E_{\mathrm{loc}}(2\omega)$, respectively. By using the Lorentz reciprocal theorem [60, 61], the relationship between the total scattered far-field of SHG from the nanoparticles $E_{\mathrm{nl}}(2\omega)$ and the local electric fields can be quantified as

$$E_{\mathrm{nl}}(2\omega) \propto \iint \chi^{(2)} E_{\mathrm{loc}}^2(\omega) E_{\mathrm{loc}}(2\omega)\, \mathrm{d}S, \tag{2.50}$$

where $\chi^{(2)}$ represents the effective surface nonlinear susceptibility. In this relation, the integration is conducted over the metal surface rather than the volume. This is because the electric fields rapidly decay upon entering the metal, which causes the nonlinearity to occur only at the surface. [62]. It can be seen from the integral that the nonlinear polarization and the mode at second harmonic must exhibit substantial spatial near-field overlap and constructive interference for optimal interaction to occur [63–65].

Assuming that the necessary overlap and constructive interference exist, it is possible to further strengthen the far-field SHG by simply increasing the magnitude of the local electric fields. The local fields described in Equation 2.50 arise from both the incident laser and the field scattered by the nanoparticles within the metasurface ($\mathbf{E}_{\mathrm{loc}}$ = $\mathbf{E}_{\mathrm{inc}}$ + $\mathbf{E}_{\mathrm{scat}}$). As a result, it is possible to significantly increase the local fields by either increasing the incident laser field amplitude or by inducing resonant modes like LSPRs or SLRs to increase the scattered fields. The latter technique highlights the compelling potential for SHG to be enhanced from the presence of multiple simultaneous resonances.

Remarkably, experimental studies have already produced multiresonant metasurfaces that utilize the single particle LSPRs [66]. Nevertheless, the broad linewidth of LSPRs, caused by significant radiative damping, still limits their potential applications in optical and electronic systems [19]. In contrast, our approach focuses on utilizing SLRs, which naturally have narrower linewidths and lower losses compared to LSPRs. Numerical simulations have demonstrated promising results, indicating that the incorporation of multiple

SLRs in nonlinear processes leads to a significant increase in conversion efficiency for both second and third-order processes [67, 68]. Building on this line of work, this Thesis goes a step further by conducting the first emprical study on how SLRs can improve multiresonant SHG [69].

Designing samples to support nonlinear processes, such as SHG, can be seen as challenging due to the strict requirements for the polarization and wavelength of relevant electric waves. In the case of type-I SHG, the multiresonant design necessitates the presence of two in-plane SLRs with orthogonal polarizations. One of these SLRs needs to be positioned in close spectral proximity to the fundamental wavelength of the nonlinear process, while the other SLR should be located at the wavelength corresponding to the SHG wavelength. Fortunately, the utilization of orthogonally polarized SLRs allows us to exploit the spatial dispersion of these resonances to generate multiresonant behavior more easily. In Chapter 2.3, the key points emphasize that by tilting the sample around two rotation axes, it becomes possible to manipulate the spectral positions of the orthogonal SLRs individually until the desired multiresonant conditions are satisfied. This way even if our samples may not demonstrate multiresonant behavior under normal incidence, we can typically still find some set of angles and wavelengths that facilitate multiresonant behavior.

3 RESEARCH METHODS

This Chapter describes the experimental methodology for studying multiresonant behavior in nonlinear optics. To begin, we present the materials and sample design parameters studied in this work and we describe our motivation for studying them. Furthermore, we explain in detail the top-down fabrication process employed to create the samples, highlighting the various stages involved and the tools and techniques employed at each stage. Lastly, we introduce the experimental setups used to determine the samples' angle-resolved linear and nonlinear responses.

3.1 Nanoparticle Array Samples

Building upon the encouraging results obtained from our computational simulations, we designed two metasurfaces, namely Sample S1 and Sample S2, to experimentally study multiresonant behaviour. These metasurfaces, spanning an area of 300 $\times$ 300 μm^2, were carefully fabricated by arranging V-shaped aluminum nanoparticles on a glass substrate with a refractive index of $n = 1.51$. The V-shaped nanoparticle design consisted of symmetrical arms measuring $l = 100$ nm in length, $w = 70$ nm in width, and $d = 30$ nm in thickness.

For both Sample S1 and Sample S2, we utilized a rectangular lattice arrangement to position the nanoparticles. The lattice constant p_y was aligned along the nanoparticle symmetry axis, which coincided with the y-axis. Conversely, the lattice constant p_x was oriented perpendicular to the nanoparticle symmetry axis, aligning with the x-axis. The distinguishing characteristic between the two samples lies in their lattice periodicities. Sample S1 exhibited periodicities of $p_x = 410$ nm and $p_y = 813$ nm, while Sample S2 had periodicities of $p_x = 398$ nm and $p_y = 813$ nm. By introducing this deliberate variation in the sample periodicities along the x-axis, we can systematically explore the system's response to multiresonant behavior under different experimental conditions. Figure 3.1 summarizes the geometry of the samples through schematic illustrations and also shows a real image captured with a scanning-electron microscope (SEM). It is worth noting that the SEM image in Figure 3.1(a) was obtained from a concurrently fabricated sample, which had the same particle dimensions but slightly different lattice periodicities ($p_x =$ 420 nm and $p_y =$ 827 nm).

The nanoparticles in Sample S1 and Sample S2 possess a symmetry that enables certain in-plane non-zero second-order susceptibility tensor components, specifically $\chi^{(2)}_{yyy}, \chi^{(2)}_{yxx},$

and $\chi^{(2)}_{xyx} = \chi^{(2)}_{xxy}$ [70]. In our work, we focus on $\chi^{(2)}_{yxx}$, which corresponds to SHG with x-polarized pump and y-polarized signal. This allows us to use orthogonal SLRs at pump and signal wavelength. Consequently, we can modify the resonant conditions at two wavelengths independently from each other.

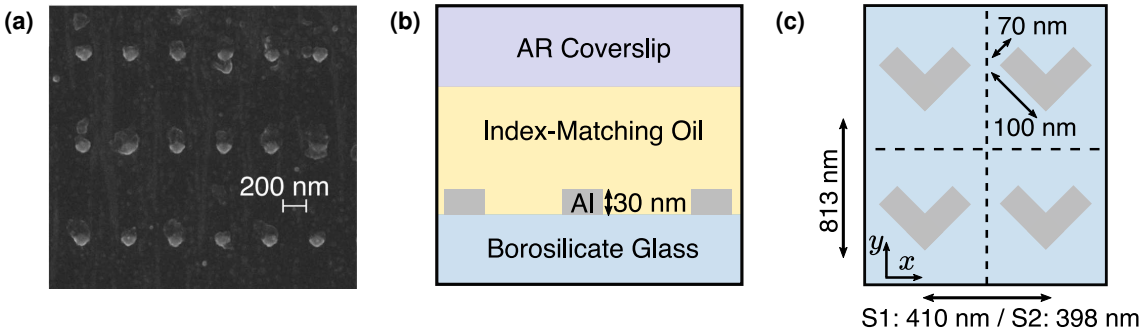

Figure 3.1. Illustration of the fabricated metamaterials through (a) a scanning-electron micrograph image and a schematic representation of the (b) metamaterial side view and (c) unit cell. Both metasurfaces comprised V-shaped aluminum nanoparticles with identical dimensions, including an arm length of 100 nm, arm width of 70 nm, and thickness of 30 nm. While the nanoparticles were arranged in a rectangular lattice, the lattice periodicities differed between the two samples.

The samples were fabricated using a well-established procedure that combines electron-beam lithography and lift-off techniques. This methodology offers precise control over the shape, size, and interparticle spacing of metallic nanostructures bound to a surface. A concise summary of the techniques utilized is visually presented in Figure 3.2. First, a 200 nm layer of PMMA-resist (MicroChem, 950k) was spin-coated on a clean glass slide (Schott Nexterion, D263T), then baked on a hot plate at 180 °C for 3 minutes and covered with a thin 10 nm aluminum layer for charge dissipation. Electron-beam lithography (Raith EBPG 5000+ 100 kV) was next used to pattern the particles onto the positive resist. The subsequent removal of the aluminum was performed using a 1% sodium hydroxide solution. Then the resist underwent development by immersing the sample in a solution consisting of a 1:3 ratio of methyl isobutyl ketone and isopropanol for a duration of 15 seconds, followed by a 30-second immersion in only isopropanol. After the resist was thoroughly dried with nitrogen, 30 nm of aluminum was deposited through electron-beam evaporation. The fabrication process continued with a lift-off process, which involved soaking the sample in acetone to remove the resist and excess metal and then cleaning the sample with sequential rinses of acetone and isopropanol. Afterward, the sample underwent a final drying process using nitrogen.

Prior to conducting the experiments, certain additions were made to the samples. These alterations included applying a thin layer of index-matching oil over the nanoparticles, which served the purpose of creating a homogeneous environment and promoting efficient diffractive coupling [71]. Furthermore, an anti-reflection (AR) coated coverslip was carefully positioned on top of the oil. The AR coating was specifically designed to operate within the wavelength range of 1000−1300 nm, effectively preventing undesired Fabry–

Pérot resonances caused by multiple reflections across various interfaces.

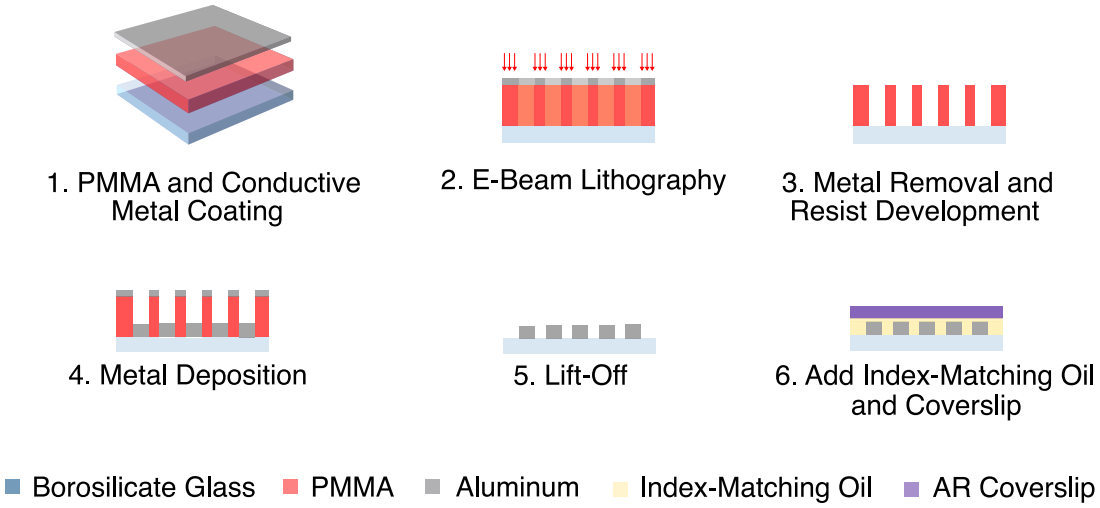

Figure 3.2. Schematic overview of the sequential steps employed in the fabrication process of our metasurfaces. These steps encompass: (1) spin-coating a PMMA-resist and metal coating, (2) drawing particles with electron-beam lithography, (3) removing metal and developing resist, (4) depositing aluminum and (5) performing lift-off using acetone. (6) The sample was finished by adding index-matching oil onto the nanoparticles with a coverslip placed on top, resulting in a homogeneous environment for the nanoparticles.

In our plasmonic research, we opted to work with aluminum instead of the more commonly used gold or silver for several reasons. Gold is unsuitable for our experiments due to its intrinsic interband transitions, which have a step-like threshold so that photons with wavelengths shorter than 500 nm are absorbed to create electron-hole pairs rather than excite surface plasmons. The utilization of gold nanoparticles would have required the displacement of LSPRs towards longer wavelengths, close to our targeted SHG wavelengths. This, in turn, would have posed a significant challenge in studying multiresonant phenomena independent of the LSPRs. Aluminum, on the other hand, exhibits a narrow interband transition occurring around 800 nm, allowing it to maintain its plasmonic properties at shorter wavelengths and enabling the existence of shorter wavelength LSPRs [72]. The choice to use aluminum instead of silver was primarily influenced by their contrasting oxidization characteristics. While aluminum has a tendency for rapid oxidation, it possesses a distinct advantage in that it naturally develops a self-limiting oxide layer. This oxide layer serves as a protective barrier, effectively impeding further oxidation and preventing the infiltration of contaminants over an extended period [73]. In contrast, silver is more susceptible to bulk oxidation, making aluminum a preferred material for our experiments. While slight oxidation may still impact the plasmonic properties of aluminum nanoparticles, our focus lies primarily on the diffractive properties of plasmonic metasurfaces, which are less affected by changes in LSPRs resulting from aluminum oxidation. In addition to the aforementioned reasons, aluminum boasts several other advantageous features that further contribute to its appeal, including its relatively low cost, abundance in nature, excellent nonlinear optical properties, and compatibility with diverse processing

techniques [74, 75].

3.2 Angle-Resolved Experimental Setups and Procedure

After the completion of sample design and fabrication, we are able to analyze the intrinsic properties of the metamaterial samples through the process of characterization. In this section, we will provide detailed explanations of the components and equipment utilized in two angle-resolved experimental setups. The primary objective of the first setup is to determine the linear transmission spectra of the metamaterial. In contrast, the second setup is designed to measure the nonlinear second-harmonic emissions of the samples.

3.2.1 Linear Setup

Broadband transmission spectra measurements are the most widely used characterization method for optical metamaterials. In plasmonics, the objective is to accurately identify the spectral positions of various resonances and assess their intensities. When the experimental transmission spectra closely match the simulated data, it is often seen as compelling evidence for the validity of the theoretical approach chosen and the success of the fabrication methods employed. In this work, we not only measure the transmission spectra at normal incidence but also at oblique angles of incidence. By studying the angle-dependent transmission spectra, we can establish the complete set of angles and wavelengths at which multiresonant behaviour can take place in the desired wavelength range for a nonlinear process to occur.

The angle-resolved extinction spectroscopy setup used in this work is depicted in Figure 3.3. In this setup, a 9 W broadband halogen lamp (SLS201 300–2600 nm, Thorlabs) was utilized as the light source. Given the high anisotropy of our metamaterials, it was imperative to have polarization control within the optical system. To achieve this, a broadband linear polarizer (LP) was positioned at the beginning of the illumination path to alter the polarization. Before reaching the sample, the incident light was passed through two achromatic lenses, AL1 (f = 40 mm) and AL2 (f = 18 mm), which reduced the size of the beam. The sample was placed on a stage that allowed rotation along a specific axis to achieve the desired tilt. After the sample, two more achromatic lenses, AL3 (f = 19.5 mm) and AL4 (f = 75 mm) were used to expand the beam. An adjustable aperture called an iris was employed to restrict the light, ensuring that only the light coming straight along the optical axis and from the correct sample was collected. Finally, a flip mirror (FM) was used to direct the light beam toward a complementary metal-oxide semiconductor (CMOS) camera for imaging the sample or toward the lens AL5 (f = 4.3 mm) and fiber-optic cable (FC) for detection by a spectrometer (SM). For measurements in the near-infrared and visible regions, we employed the NIR128L-1.7 (Control Development) and AvaSpec-ULS-RS-TEC (Avantes) SMs, respectively.

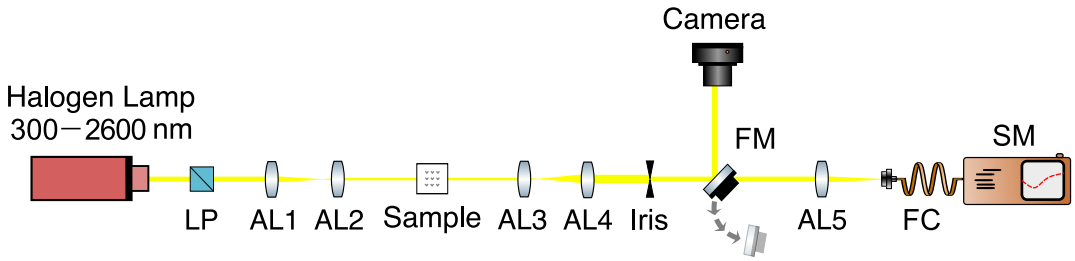

Figure 3.3. A schematic representation of the optical setup utilized for measuring linear transmission. The following notations are used: LP - linear polarizer, AL - achromatic lens (AL1, f = 19.5 mm; AL2, f = 18 mm; AL3, f = 19.5 mm; AL4, f = 75 mm; AL5, f = 4.3 mm), FM - flip mirror, FC - fiber-optic cable, SM - spectrometer.

In accordance with standard practices, the measurement of transmission spectra requires the acquisition of appropriate dark and reference measurements. The dark spectrum quantifies the influence of background light. To obtain the dark spectrum, a spectrum is recorded while intentionally blocking the halogen optical beam path from reaching the spectrometer. This is accomplished in our experimental setup by positioning the flip mirror in front of the spectrometer so that the light is redirected toward the camera instead. Conversely, the reference measurement entails the recording of a spectrum as the optical beam path passes through a distinct region of the sample consisting solely of the substrate. This allows us to exclusively evaluate the properties specific to the nanostructured layer.

3.2.2 Nonlinear Setup

Having obtained data from transmission measurements that capture the specific angles and wavelengths associated with multiresonant behavior, we can then proceed to investigate the influence of such behavior on SHG. The experimental setup for SHG characterization is depicted in Figure 3.4. The setup includes a Ti:sapphire laser that produces linearly polarized short pulses with a duration of 140 fs. The generated pulses feature a repetition rate denoted as ν_{rep}, which is set at 80 MHz, and they operate at a wavelength of 800 nm. The laser's output serves as the pump source for an OPO. The primary role of the OPO is to enable access to wavelengths in the range of 1000 - 1300 nm. Incidentally, while achieving this, the OPO also modifies the pulse duration of the light, denoted as τ_{p}, extending it to 200 fs.

To measure the input optical power indirectly, voltage is measured by a reference germanium photodiode (PD). This voltage reading is then utilized to make small adjustments to the rotation of a half-wave retardation plate (HWP1). By working together with a linear polarizer (LP1), these two components act as an optical attenuator that ensures a safe and constant input power is maintained across the entire range of wavelengths employed in the experiment.

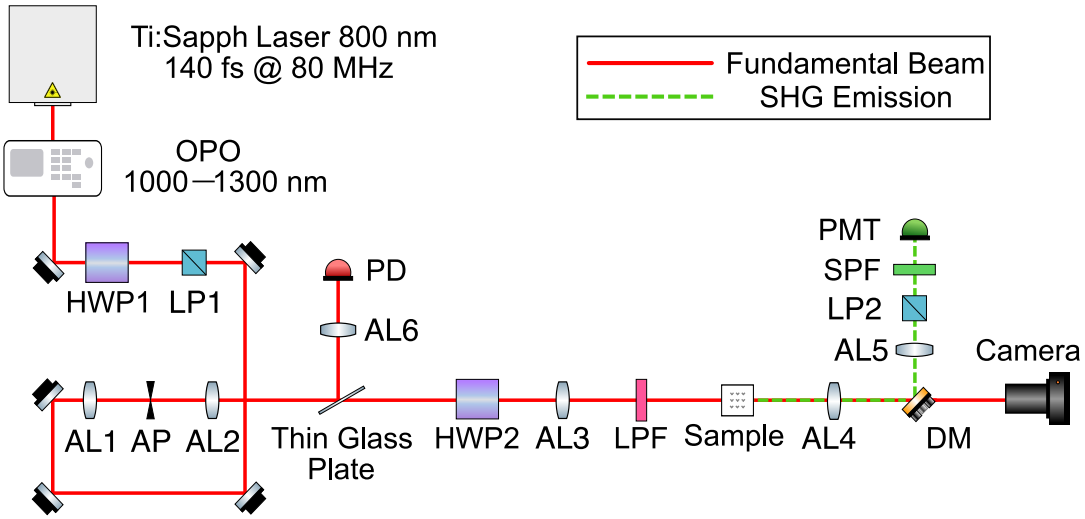

Figure 3.4. The setup for measuring angle-resolved SHG emissions from a nonlinear sample comprised the following components: a laser (Ti:Sapph), an optical parametric oscillator (OPO), half-wave plates (HWP), linear polarizers (LP), an achromatic lens system (AL1, f = 30 mm; AL2, f = 150 mm; AL3, f = 500 mm; AL4, f = 50 mm; AL5, f = 150 mm; AL6, f = 75 mm), an aperture (A), a photomultiplier tube (PMT), a long-pass filter (LPF), a short-pass filter (SPF), a dichroic mirror (DM), and a photodiode (PD). The fundamental beam is depicted by the solid red line, and the path of SHG emission is indicated by the dashed green line.

After passing through the optical attenuator, the incident light undergoes expansion using the first and second achromatic lenses (AL), AL1 (f = 30 mm) and AL2 (f = 150 mm), respectively. Utilizing beam expansion is crucial as it serves two key purposes in the setup. Firstly, it enables a wider field-of-view during sample imaging, allowing for a broader coverage area. Secondly, it aids in the creation of a smaller laser focal spot diameter at a later stage in the setup when the light hits the sample. Within the beam expander, the pinhole serves as a low-pass spatial filter and consequently ensures a high-quality beam profile for the pump beam. This spatially filtered and expanded light is then directed to HWP2, which sets the orientation of the incident beam's polarization plane. Following this, lens AL3 (f = 500 mm) focuses the fundamental wavelength onto the sample. Prior to reaching the sample, the incident light undergoes filtration using a long-pass filter (LPF). This precautionary measure makes certain that the detected SHG signal originates solely from the specific sample being studied, by filtering out residual light from the original Ti:Sapphire laser and its harmonics. It also prevents the inclusion of SHG signals that may be generated by earlier optical components in the setup.

To adjust the angle of incidence, the sample was set onto a motorized rotation stage. This specialized stage incorporated a small single-axis goniometer, designed for fine-tuning the sample's angular orientation about one axis. This goniometer was strategically placed on top of a 3-axis translational stage, which allowed for the movement of the sample in three-dimensional space. Adding to the control of this setup, a motor-driven rotating platform was positioned beneath the translational stage, granting an additional axis for fine-tuning the angular orientation of the sample.

The SHG signal is collected by lens AL4 (f = 50 mm), directed to the detection path through a dichroic mirror (DM), and focused onto the active area of a photomultiplier tube (PMT) module by lens AL5 (f = 150 mm). The signal is filtered by a short-pass filter (SPF) and polarizer LP2 to ensure the correct wavelength and polarization state of SHG before reaching the PMT. The fundamental light that is passed through the DM is utilized in visualizing the sample plane with a CMOS camera in between measurements. To transform the detected SHG signals to absolute powers, the PMT was calibrated against a femtowatt power meter (RM9-PD, Ophir), and a copper(II) acetylacetonate crystal with known nonlinear properties was used as a calibration material. The outcome of this calibration revealed that in our experimental setup, one PMT count equates to 5.2×10^{-18}W. To reduce the likelihood of damage to Samples S1 and S2, we made the decision to use an input power of 75 mW for our nonlinear experiments. Furthermore, as a protective measure, we introduced a shutter to safeguard the samples when measurements were not actively being conducted.

With knowledge of the experimental setup and average input power, we are able to estimate the intensity of the fundamental laser beam, denoted as $I_\omega = P_\omega/A_\mathrm{b}$. This parameter holds significant importance in nonlinear optical processes. To determine the peak intensity of our setup, we have to first evaluate the beam diameter at the sample plane using basic Gaussian optics. The beam diameter of a focused Gaussian beam can be estimated using the equation $d = \frac{4\lambda f}{\pi d_0}$, where f is the focal length of the lens, d_0 is the beam diameter at the focusing lens and λ is the laser wavelength [76]. In our experiment, the beam diameter ($\frac{1}{e^2}$ of maximum intensity) at the OPO output was initially 2 mm, which was then increased to 1 cm by lenses L1 and L2. By focusing the laser beam (λ = 1200 nm) with lens AL3 (f = 500 mm), the beam diameter at the sample plane was reduced to 76 μm. We also used a CMOS camera to verify the beam size by comparing the laser spot to the sample arrays which we already know to cover an area of 300$\times$300 μm^2, and the resulting measurement was identical to our previous calculated estimate. With these parameters in hand, we can estimate the peak intensity of a femtosecond laser pulse (P_avg = 75 mW, τ_p = 200 fs, ν_rep = 80 MHz) as

$$I_\mathrm{peak} = \frac{P_\mathrm{peak}}{A_\mathrm{b}} = \frac{P_\mathrm{avg}}{1.763\tau_\mathrm{p}\nu_\mathrm{rep}A_\mathrm{b}} = 117\ \mathrm{MW/cm^2}, \tag{3.1}$$

where $A_\mathrm{b} = \frac{\pi(d/2)^2}{2} \approx 2268\ \mu\mathrm{m}^2$ is the area of the laser beam. Although the spatial profile of laser beams commonly takes the form of a Gaussian profile, the temporal profile observed in ultrashort pulses generated by mode-locked lasers typically takes the form of a squared hyperbolic secant line profile [2]. For this reason, we include a factor of 1.763 to determine the full-width at half maximum pulse duration of a squared hyperbolic secant pulse shape based on its pulse duration.

4 RESULTS AND DISCUSSION

In this Chapter, we will reveal the results of the experiments outlined in the previous section. We will first show the experimental findings of the transmission spectra under both normal and oblique angles of incidence. This is followed by the presentation of the SHG emissions. The nonlinear results will be rigorously analyzed and discussed in conjunction with the linear results, in an effort to draw conclusive insights regarding the influence of multiresonant behavior on nonlinear optics.

4.1 Transmission Measurements

The transmission spectra were evaluated at normal incidence for both Samples S1 and S2 in the visible and near-infrared regions with two orthogonal polarizations of light, as depicted in Figure 4.1. The transmission spectra reveal the presence of narrow resonance peaks, attributed to the SLRs. We utilize a red line to denote the transmission spectrum that occurs as a result of x-polarized incident light, while a blue line is employed to indicate the transmission of the sample when subjected to y-polarized light. With the range of lattice periods and wavelengths covered in this experimental work, four distinct resonant modes emerged that were identical to the modes observed in our previous simulations. We successfully excited two first-order perpendicular SLRs, namely the y-polarized SLR$_{(\pm1,0)}$ and x-polarized SLR$_{(0,\pm1)}$, along with one second-order perpendicular SLR$_{(0,\pm2)}$. We were also able to excite SLR$_{(\pm1,\pm1)}$ in a diagonal direction with both polarizations.

When illuminated by x-polarized light, Samples S1 and S2, which share the same lattice periodicity in the y-direction, exhibit the first and second-order x-polarized perpendicular SLR at the same location. These resonances peak at wavelengths $\lambda_{(0,\pm1)}$ = 1220 nm and $\lambda_{(0,\pm2)}$ = 628 nm. However, the different periodicity in the x-direction of the two samples results in varying spectral locations for the other SLRs. For Sample S1, the y-polarized perpendicular SLR is centered at $\lambda_{(\pm1,0)}$ = 626 nm and for Sample S2, it is at $\lambda_{(\pm1,0)}$ = 610 nm when the samples are illumated with y-polarized light. For both polarizations diagonal SLRs occurs at $\lambda_{(\pm1,\pm1)}$ = 560 nm for S1 and $\lambda_{(\pm1,\pm1)}$ = 546 nm for S2.

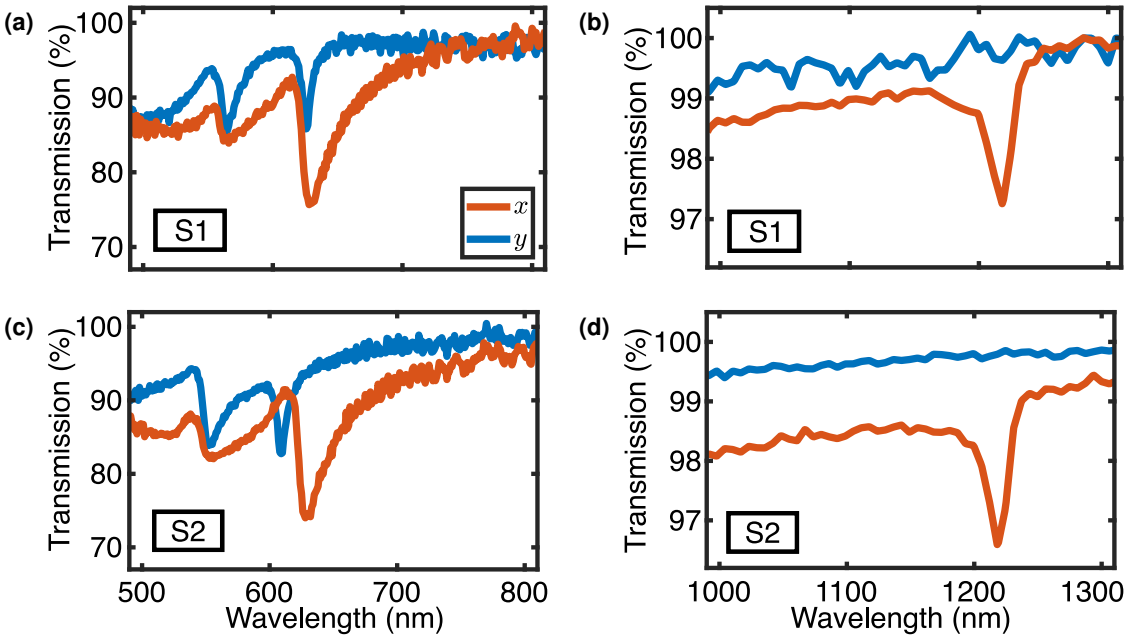

Figure 4.1. Transmission spectra measured from Sample S1 (a)–(b) and Sample S2 (c)–(d) in the visible and near-infrared wavelengths at normal incidence. Utilizing x- (red) and y- (blue) input polarizations led to the excitation of four resonant modes for both Sample S1 and Sample S2.

We have carefully designed our experimental setup and chosen our samples with the intention of achieving SHG via the tensor component $\chi^{(2)}_{yxx}$. This process necessitates the use of an x-polarized pump and a y-polarized signal. To transition to a multiresonant state, we must align the pump wavelength with the longer-wavelength, x-polarized $\text{SLR}_{(0,\pm1)}$ and the signal with either the y-polarized $\text{SLR}_{(\pm1,0)}$ or the diagonal $\text{SLR}_{(\pm1,\pm1)}$ that occur at shorter wavelengths. These alignments set forth the circumstances for multiply-resonant operation, defined by the resonance wavelengths $\lambda_x(\theta_y)$ and $\lambda_y(\theta_x)$. This condition can be expressed as

$$\lambda_x(\theta_y) = 2\lambda_y(\theta_x), \tag{4.1}$$

where θ_x and θ_y highlight that the SLR wavelengths are adjusted by tilting the sample appropriately. In practical terms, this means that we illuminate the sample at an angle θ_y, while the SHG signal is collected at an angle θ_x with respect to the sample plane.

With this understanding, we proceeded to conduct extinction spectra measurements at oblique incidence angles that vary from -4 degrees to 4 degrees with x-polarization, and -14 degrees to 14 degrees with y-polarization. The results of this experiment for Samples S1 and S2 are depicted in Figures 4.2 and 4.3, where the SLR extinction is plotted as a function of both the angle of incidence and the wavelength of incident light. To validate our experimental results, we superimposed solid dots on the dispersion diagrams. These dots indicate the positions of the Rayleigh anomalies as computed through Equation 2.10, demonstrating a high degree of agreement between our experimental results and

the ELA predictions. Additionally, as expected for both samples, the negative and positive angles of incidence display a similar linear response within the limits of our experimental precision.

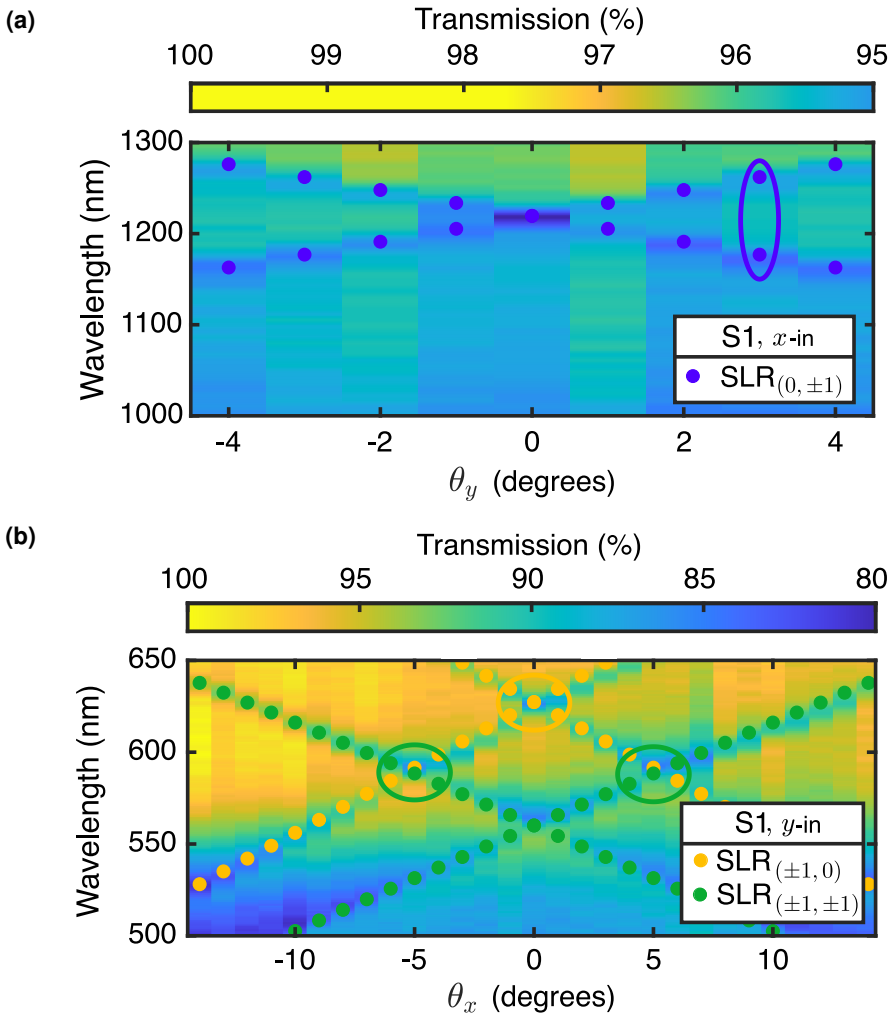

Figure 4.2. Dispersion diagram for Sample S1 was obtained by measuring transmission as a function of incident angle and wavelength for (a) x- and (b) y-polarized incident light. At normal incidence, S1 exhibits first-order perpendicular SLRs, which are x-polarized at 1220 nm (blue dots), and y-polarized at 626 nm (yellow dots). Additionally, first-order diagonal SLRs occur at 560 nm (green dots). Deviation from their normal incidence values occurs when the sample is tilted.

When examining the potential for multiresonant behavior, it's noteworthy to highlight the spectral positioning of the resonances. As required, the x-polarized resonance can be found within a spectral window spanning 1000–1300 nm. This range demonstrates a close alignment with the fundamental wavelength selected for use in our SHG measurements. Simultaneously, the pair of y-polarized resonances are found near the spectral window of 500–650 nm, which falls within the signal wavelength region.

In the case of Sample S1, it is not possible to meet the multiresonant conditions at a normal incidence. Fortunately, we can utilize the dispersions of SLRs to achieve the

conditions by tilting the sample appropriately. For instance, if we adjust the angle to $\theta_y = \pm 3°$, we notice that the x-polarized $\text{SLR}_{(0,\pm1)}$ is split into two peaks located at 1180 nm and 1252 nm within the fundamental wavelength range. This particular configuration is highlighted with a solid blue ellipse in Figure 4.2(a). In such a setting, and with $\theta_x = 0°$, we are conveniently able to meet the multi-resonant conditions with the y-polarized $\text{SLR}_{(\pm1,0)}$ situated at the SHG wavelength of 626 nm and the fundamental beam at 1252 nm. Furthermore, we can construct a triply resonant metasurface at $\theta_x = \pm 5°$. Here, the y-polarized $\text{SLR}_{(\pm1,0)}$ overlaps with the diagonal $\text{SLR}_{(\pm1,\pm1)}$ at the SHG wavelength of 590 nm while the pump is centered at 1180 nm [1]. The regions signifying these two resonant conditions are distinctly marked in Figure 4.2(b) with yellow and green ellipses, respectively.

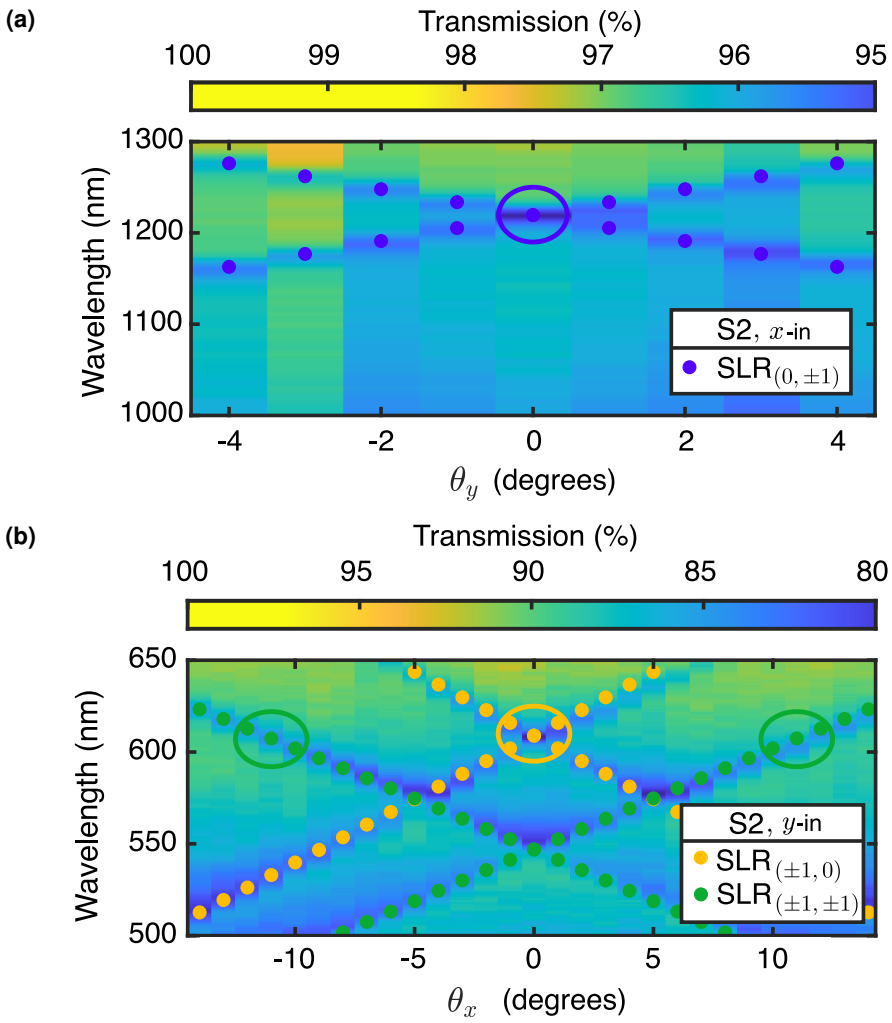

Figure 4.3. Dispersion diagram for Sample S2 with (a) x- and (b) y-polarized incident light. At normal incidence, Sample S2 demonstrates first-order perpendicular SLRs which are x-polarized at 1220 nm (blue dots) and y-polarized at 610 nm (yellow dots). First-order diagonal SLRs also occur at 546 nm (green dots). The SLRs can move from their normal incidence values by tilting the sample along a specific axis.

[1] It is assumed here that the modest θ_y shift has minimal impact on the spectral location of the diagonal SLR. As inferred from Figure 2.8 in the LSA, the diagonal SLR's splitting rate with respect to θ_y is slower compared to θ_x. For a tilt of $\theta_y = 3°$, the estimated spectral shift of the SLR is less than 8 nm.

Unlike Sample S1, the multiresonant conditions can be achieved at normal incidence ($\theta_x = \theta_y = 0°$) for Sample S2. In this situation, the x-polarized $SLR_{(0,\pm1)}$ at the pump wavelength of 1220 nm overlaps with the y-polarized $SLR_{(\pm1,0)}$ at the SHG wavelength of 610 nm. Additionally, by tilting the sample about the y-axis and setting $\theta_x = \pm 11°$, the diagonal $SLR_{(\pm1,\pm1)}$ shifts to 610 nm, thereby also fulfilling the multiresonant condition. These conditions are marked in Figure 4.3 with solid circles.

To ensure that our multiresonant conditions are driven exclusively by SLRs without any interference from LSPRs, we estimated the location of individual LSPRs. When nanoparticles are arranged randomly, the long-range interactions between particles effectively average out [77]. Consequently, in large arrays, the resonance accurately reflects the form and location of the single particle resonance. To explore this for our samples, we created a sample with the same nanoparticles as in Samples S1 and S2, but dispersed randomly across the metasurface. To amplify the signal, we decreased the average unit cell size by a factor of four in relation to the original samples. The linear transmission spectra of this random lattice are showcased in Appendix's Figure A.1. It reveals a prominent LSPR at normal incidence, which varies based on the incident polarization. Specifically, the LSPR peak was observed at 550 nm for x-polarized light and 475 nm for y-polarized light, with a linewidth of approximately 100 nm. Though these resonances are close to our SHG signal wavelength, it's important to note that the LSPR generated by y-polarized light does not coincide with any of our chosen multiresonant wavelengths in the visible wavelength region. Therefore, any potential enhancement in the SHG emissions would solely result from the influence of SLRs.

4.2 Second-Harmonic Generation Measurements

In the previous section, we identified several feasible multiresonant angle-wavelength combinations from the SLR dispersion graphs in Figure 4.2 and Figure 4.3. Naturally, the next step is to experimentally validate these values by measuring the on-and-off resonance second-harmonic enhancement. To exemplify multiply-resonant operation for Sample S1, we adjusted $\theta_y = 3°$ and we measured the SHG (corresponding to $\chi^{(2)}_{yxx}$) as a function of incident angle θ_x and pump wavelength. The SHG emissions are presented in Figure 4.4 and the results highlight a direct link between linear and nonlinear regimes. The nonlinear emission pattern resembles the dispersion of y-polarized SLRs shown in Figure 4.2 and it is equivalent for positive and negative angles. The signal reaches its highest value when Sample S1 contains a triple resonance due to the presence of both the diagonal and perpendicular y-polarized SLRs. In these specific positions, the SHG emission is eight times greater compared to the off-resonance signal. The emission peaks at a power of 5.7 fW, which corresponds to a 7.6×10^{-14} conversion efficiency.

While overlapping SLRs create stronger resonance than separate ones, these results can't confirm that the strong signals are due to a multiresonant metasurface. If multiresonant coupling is present, the SHG emissions at the two different pump wavelengths

should be very prominent, regardless of changes in θ_x. However, the SLRs near the pump wavelength of 1252 nm and 1180 nm are significantly weak when compared to the normal incidence x-polarized SLR$_{(0,\pm1)}$, making it difficult to observe constant enhancement from the two pump wavelengths at different angle of incidences in the xz-plane. The SHG enhancement in Figure 4.4 could be interpreted as resulting only from the overlap of y-polarized SLR$_{(\pm1,0)}$ and diagonal SLR$_{(\pm1,\pm1)}$ near the signal wavelength.

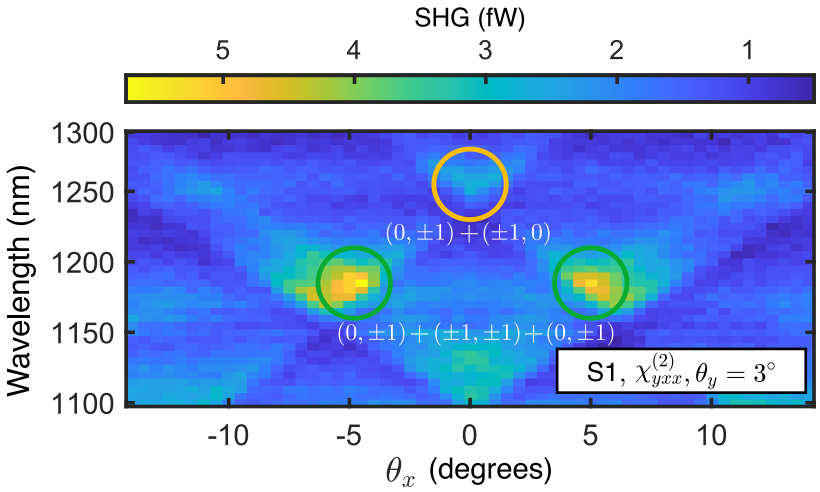

Figure 4.4. Contour plot of SHG emission as a function of incident angle and pump wavelength for Sample S1. The sample was set to $\theta_y = 3°$ and then tilted with respect to the x-axis by the amount θ_x. At three distinct combinations of wavelength and angle, the emission of SHG is significantly enhanced. At θ_x = 0° (yellow circle), we have x-polarized and y-polarized perpendicular SLRs enhancing the produced SHG at 1252 nm. We see again at $\theta_x = \pm5°$ SHG enhancement (green circles), but this time it is due to the x-polarized perpendicular SLR occurring at 1180 nm and the diagonal SLR at 590 nm.

To demonstrate the multiply-resonant operation of our metasurfaces more clearly, we measured the SHG emission of S2 by first tilting the sample to $\theta_y = 0°$. Because we stay at normal incidence with respect to the yz-plane, we have a stronger x-polarized SLR$_{(0,\pm1)}$ as the peak is not split into two smaller ones, as in previous measurements. Figure 4.5 shows the SHG emission of Sample S2 as a function of incident angle θ_x ranging from -15° to 15° and pump wavelength ranging from 1100–1300 nm. In this Figure, a constant increase in SHG efficiency is visible for all θ_x values at the 1220 nm fundamental wavelength. The distinct horizontal line of approximately 2.5 fW in SHG indicates the impact of the pump wavelength and confirms multiresonant behavior. The SHG pattern elsewhere conforms to the dispersion of y-polarized SLRs. Notably, the highest signal was attained under multiresonant conditions at 1220 nm and $\theta_x = [0°, \pm11°]$, yielding a 10-fold increase in SHG and a peak emission power of 5.7 fW, equivalent to a conversion efficiency of 7.7×10^{-14}.

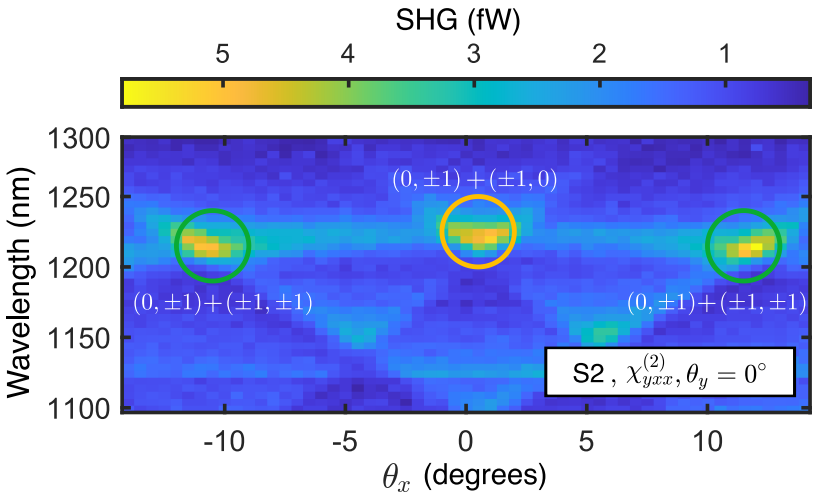

Figure 4.5. SHG emission of Sample S2 as a function of incident angle and pump wavelength. The sample was set to θ_y = 0° and then tilted with respect to the x-axis. As a result, the SH emission is enhanced at 1220 nm at three different angles. Firstly, at θ_x = 0° (yellow circle), the enhancement occurs due to the x- and y-polarized perpendicular SLRs. Secondly, at $\theta_x = \pm5°$ (green circles), the enhancement is a result of the x-polarized perpendicular SLR and the diagonal SLR.

The SHG signal levels in this study appear modest when compared to prior research on plasmonic nanostructures [22, 23]. One significant reason for this is the relatively low Q-factor SLRs located at the pump wavelengths, which have an extinction below 5% and a Q-factor close to 60 at normal incidence. In principle, enhancing the Q-factor could be achieved by enlarging the nanoparticles to facilitate stronger inter-particle coupling in the array. However, for this study, such an approach wasn't viable. The increased size of the nanoparticles would cause the LSPRs to move into the nonlinear signal wavelength spectrum, preventing the exclusive use of SLRs to achieve multiresonant behavior. A more tangible strategy for enhancing the low Q-factors becomes clear from analyzing the SEM image shown in Figure 3.1. This image points towards non-uniform nanoparticle geometries in our samples, likely due to the surface irregularities caused by the aluminum evaporation process [78]. Although these variations in geometry don't seem to negatively influence the dispersion or spectral positioning of the SLRs, improving them could further enhance inter-particle interactions [79]. Separately, it's important to remember that SHG is already highly sensitive to nanoparticle symmetry. Even slight structural changes in the nanoparticles can lead to significant alterations in the SHG output, both in terms of its nature and magnitude. Thus, the observed shape irregularities might have contributed to reduced SHG emissions compared to potentially optimal shapes.

Once the Q-factors of the SLRs are optimized, further steps can be taken to enhance the overall nonlinear signal in our transparent samples. One promising strategy is layering multiple metasurfaces. Although this method is not trivial, phase-matched stacked metasurfaces offer a direct path for amplifying weaker nonlinear signals [31]. Additional methods, such as employing multi-pass pumping schemes or crafting metasurfaces capa-

ble of enduring higher-intensity pumping, could also be explored for signal enhancement [80, 81].

Unfortunately, limited time and computational resources prevented us from simulating nonlinear responses for comparison with our experimental SHG emissions. However, these calculations could have been done using the help of FDTD or DDA. To estimate the far-field SHG emission for periodic metasurfaces, one can simulate the field profiles of a nanoparticle with FDTD and then calculate mode-overlap integrals [82]. Additionally, the angle-dependent nonlinear responses could be estimated by employing a nonlinear DDA method [68]. It is important to note that the latter method treats individual nanoparticles as point-like scatterers, which unfortunately restricts the possibility of conducting mode-overlap calculations. Nonetheless, this approach is computationally less demanding compared to techniques based on full-wave simulations.

5 CONCLUSION

Inspired by the trend of increasing miniaturization, we investigated the nonlinear responses of multiresonant plasmonic metasurfaces. This work brings novel contributions to the field by utilizing the dispersion of relatively high Q-factor SLRs to spectrally shift the SLRs to the pump and signal wavelengths of a nonlinear process, thereby creating multiresonant behavior. Successful implementation of our approach on two distinct samples revealed that the presence of multiple SLRs led to a prominent enhancement of SHG emission via the amplification of local electric fields.

Achieving these results involved the careful completion of multiple preparatory steps to ensure appropriate experimentation and accurate analysis of the multiresonant behavior. We approached the work, by first conducting a comprehensive study of the dispersion of SLRs. We used a collection of the most relevant theoretical, analytical, and numerical modeling techniques to model the linear optical response of nanoparticles. Our analysis of nanoparticles arranged into a rectangular lattice revealed comparable SLR behavior across all the models, which included ELA, LSA, and FDTD. The results clearly illustrate that by rotating a sample about an axis, the spectral locations of SLRs can be changed if the rotation happens about the axis that is orthogonal to the direction that the in-plane perpendicular SLR travels. This allows us to independently control SLRs that are orthogonally polarized, enabling us to utilize this capability for the purpose of constructing a tunable multiresonant sample that could potentially enhance nonlinear signals.

Drawing inspiration from the promising results of our simulations, we designed and fabricated multiresonant metasurfaces. By employing electron-beam lithography and lift-off processes, we deposited noncentrosymmetric V-shaped aluminum nanoparticles onto a glass substrate, with the specific purpose of achieving type-I SHG. The nanoparticles were arranged in a rectangular lattice pattern on both samples, albeit with varying lattice periods. This deliberate manipulation of the lattice periodicity allowed us to systematically assess the multiresonant behavior of the system under diverse experimental conditions, with the ultimate goal of obtaining reliable and reproducible results in relation to the impact of multiresonant behavior on nonlinear phenomena.

After completing the fabrication of the samples, we proceeded to thoroughly characterize the linear properties of the metasurfaces. This involved conducting transmission spectra measurements at normal incidence with varying polarizations to accurately identify the resonances present in our samples. Through this process, we were able to identify four distinct in-plane SLRs within the wavelength range accessible with our experimental

setup. From these four options, we carefully selected three first-order SLRs for further study due to their close spectral positioning to either the fundamental laser wavelength or the corresponding SHG signal wavelength. The chosen SLRs offer the added advantage of independent spectral location tuning by simply rotating the sample, providing us with enhanced flexibility and control over the experimental setup to create desired multiresonant behavior.

Next, we conducted spatial dispersion measurements for the three selected in-plane SLRs. This involved measuring the transmission as a function of pump wavelength and angle of incidence. Since our samples were designed for type-I SHG, where they exhibit a y-polarized SHG signal when pumped with an x-polarized input, we conducted dispersion measurements with orthogonal input polarizations for the two wavelength regions of interest. By carefully analyzing the dispersion diagrams, we could easily identify several potential multiresonant wavelength and incident angle combinations for both samples.

Finally, in the culmination of our research efforts, we experimentally tested the effectiveness of our multiresonant conditions on SHG. This involved finely tuning the pump wavelength and optimizing the angle of incidence to its optimal value, followed by measuring the emissions of SHG. Our findings unveiled multiple instances where simultaneous SLRs at both the pump and signal wavelengths significantly amplified the SHG response. Under multiresonant conditions, the SHG emissions reached their peak, exhibiting a remarkable 10-fold enhancement compared to non-multiresonant conditions. This enhancement resulted in a conversion efficiency of 7.7×10^{-14} with a peak emission power of 5.7 fW.

In summary, we experimentally demonstrated the applicability of multiresonant metasurfaces to enhance nonlinear effects. Despite the modest signal levels, our results unveil a novel mechanism for achieving tunable SHG enhancement. By tilting the sample, we are able to modulate the multiply-resonant wavelength, thereby fine-tuning the wavelength at which the strongest SHG response is achieved. This post-fabrication tunability presents a significant opportunity for improving a range of nonlinear effects, including DFG, spontaneous parametric down-conversion (SPDC), four-wave mixing (FWM) and third-harmonic generation (THG) without the need for phase-matching considerations. This exciting prospect opens up new avenues for exploration and experimentation. Furthermore, while our study focused on SHG from V-shaped aluminum nanoparticles on a glass substrate, the concept of multiresonant behavior could be harnessed to amplify light–matter interactions in different types of nonlinear metasurfaces and metamaterials. In fact, the proposed approach may be particularly effective in enhancing the nonlinear responses of all-dielectric metasurfaces, which have the potential to support higher Q-factor resonances compared to current metal–dielectric metasurfaces [83, 84]. Ultimately, we believe that our methodology presents a general and transformative approach to significantly enhance nonlinear effects in metasurfaces and it is a step forward in the journey towards smaller, more efficient nonlinear devices.

REFERENCES

[1] Y. Shen. *The Principles of Nonlinear Optics*. Pure & Applied Optics Series. Wiley, 1984.

[2] G. P. Agrawal. *Nonlinear Fiber Optics*. USA: Elsevier, 2019.

[3] R. W. Boyd. *Nonlinear Optics*. USA: Academic Press, 2008.

[4] P. A. Franken, A. E. Hill, C. W. Peters and G. Weinreich, “Generation of Optical Harmonics," *Physical Review Letters*, **7**, 118 (1961).

[5] G. Eckhardt, R. W. Hellwarth, F. J. McClung, S. E. Schwarz, D. Weiner and E. J. Woodbury, “Stimulated Raman Scattering From Organic Liquids," *Physical Review Letters*, **9**, 455 (1962).

[6] R. W. Terhune, P. D. Maker and C. M. Savage, “Optical Harmonic Generation in Calcite," *Physical Review Letters*, **8**, 404 (1962).

[7] M. Bass, P. A. Franken, J. F. Ward and G. Weinreich, “Optical Rectification," *Physical Review Letters*, **9**, 446 (1962).

[8] T. H. Maiman, “Stimulated Optical Radiation in Ruby," *Nature*, **187**, 493–494 (1960).

[9] Y. R. Shen, “Surface Properties Probed by Second-Harmonic and Sum-Frequency Generation," *Nature*, **337**, 519–525 (1989).

[10] G. O. Clay, A. C. Millard, C. B. Schaffer, J. Aus-der-Au, P. S. Tsai, J. A. Squier and D. Kleinfeld, “Spectroscopy of Third-Harmonic Generation: Evidence for Resonances in Model Compounds and Ligated Hemoglobin," *Journal of the Optical Society of America B*, **23**, 932–950 (2006).

[11] M. Taghinejad and W. Cai, “All-Optical Control of Light in Micro- and Nanophotonics," *ACS Photonics*, **6**, 1082–1093 (2019).

[12] Y. Wang, K. D. Jöns and Z. Sun, “Integrated Photon-Pair Sources with Nonlinear Optics," *Applied Physics Reviews*, **8**, 011314 (2021).

[13] N. Kotov, “Bioimaging: The Only Way Is Up," *Nature Materials*, **10**, 903–904 (2011).

[14] A. V. Kachynski, A. Pliss, A. N. Kuzmin, T. Y. Ohulchanskyy, A. Baev, J. Qu and P. N. Prasad, “Photodynamic Therapy by In Situ Nonlinear Photon Conversion," *Nature Photonics*, **8**, 455–461 (2014).

[15] J. Deinert, D. Alcaraz Iranzo, R. Pérez, X. Jia, H. A. Hafez, I. Ilyakov, N. Awari, M. Chen, M. Bawatna, A. N. Ponomaryov, S. Germanskiy, M. Bonn, F. H. Koppens, D. Turchinovich, M. Gensch, S. Kovalev and K.-J. Tielrooij, “Grating-Graphene Metamaterial as a Platform for Terahertz Nonlinear Photonics," *ACS Nano*, **15**, 1145–1154 (2021).

[16] T. Hu, C.-K. Tseng, Y. H. Fu, Z. Xu, Y. Dong, S. Wang, K. H. Lai, V. Bliznetsov, S. Zhu, Q. Lin and Y. Gu, “Demonstration of Color Display Metasurfaces via Immersion Lithography on a 12-Inch Silicon Wafer," *Optics Express*, **26**, 19548–19554 (2018).

[17] T. Lee, C. Lee, D. K. Oh, T. Badloe, J. G. Ok and J. Rho, “Scalable and High-Throughput Top-Down Manufacturing of Optical Metasurfaces," *Sensors*, **20**, 4108 (2020).

[18] A. Ashkin, G. Boyd and J. Dziedzic, “Resonant Optical Second Harmonic Generation and Mixing," *IEEE Journal of Quantum Electronics*, **2**, 109–124 (1966).

[19] M. Kauranen and A. V. Zayats, “Nonlinear Plasmonics," *Nature Photonics*, **6**, 737–748 (2012).

[20] V. G. Kravets, A. V. Kabashin, W. L. Barnes and A. N. Grigorenko, “Plasmonic Surface Lattice Resonances: A Review of Properties and Applications," *Chemical Reviews*, **118**, 5912–5951 (2018).

[21] M. S. Bin-Alam, O. Reshef, Y. Mamchur, M. Z. Alam, G. Carlow, J. Upham, B. T. Sullivan, J.-M. Ménard, M. J. Huttunen, R. W. Boyd and K. Dolgaleva, “Ultra-High-Q Resonances in Plasmonic Metasurfaces," *Nature Communications*, **12**, 974–982 (2021).

[22] L. Michaeli, S. Keren-Zur, O. Avayu, H. Suchowski and T. Ellenbogen, “Nonlinear Surface Lattice Resonance in Plasmonic Nanoparticle Arrays," *Physical Review Letters*, **118**, 243904 (2017).

[23] D. C. Hooper, C. Kuppe, D. Wang, W. Wang, J. Guan, T. W. Odom and V. K. Valev, “Second Harmonic Spectroscopy of Surface Lattice Resonances," *Nano Letters*, **19**, 165–172 (2019).

[24] R. Czaplicki, A. Kiviniemi, M. J. Huttunen, X. Zang, T. Stolt, I. Vartiainen, J. Butet, M. Kuittinen, O. J. F. Martin and M. Kauranen, “Less Is More: Enhancement of Second-Harmonic Generation from Metasurfaces by Reduced Nanoparticle Density," *Nano Letters*, **18**, 7709–7714 (2018).

[25] B. K. Canfield, S. Kujala, K. Jefimovs, J. Turunen and M. Kauranen, “Linear and Nonlinear Optical Responses Influenced by Broken Symmetry in an Array of Gold Nanoparticles," *Optics Express*, **12**, 5418–5423 (2004).

[26] R. Czaplicki, A. Kiviniemi, J. Laukkanen, J. Lehtolahti, M. Kuittinen and M. Kauranen, “Surface Lattice Resonances in Second-Harmonic Generation from Metasurfaces," *Optics Letters*, **41**, 2684–2687 (2016).

[27] C. Hubert, L. Billot, P.-M. Adam, R. Bachelot, P. Royer, J. Grand, D. Gindre, K. D. Dorkenoo and A. Fort, “Role of Surface Plasmon in Second Harmonic Generation from Gold Nanorods," *Applied Physics Letters*, **90**, 181105 (2007).

[28] P. Hofmann. *Solid State Physics: An Introduction*. Wiley, 2015.

[29] R. Guo, M. Necada, T. K. Hakala, A. I. Väkeväinen and P. Törmä, “Lasing at K Points of a Honeycomb Plasmonic Lattice," *Physical Review Letters*, **122**, 013901 (2019).

[30] W. Cai, U. K. Chettiar, H.-K. Yuan, V. C. De Silva, A. V. Kildishev, V. P. Drachev and V. M. Shalaev, “Metamagnetics with Rainbow Colors," *Optics Express*, **15**, 3333–3341 (2007).

[31] T. Stolt, J. Kim, S. Héron, A. Vesala, Y. Yang, J. Mun, M. Kim, M. J. Huttunen, R. Czaplicki, M. Kauranen, J. Rho and P. Genevet, “Backward Phase-Matched

Second-Harmonic Generation from Stacked Metasurfaces," *Physical Review Letters*, **126**, 033901 (2021).

[32] K. Aydin, I. Bulu and E. Ozbay, “Subwavelength Resolution with a Negative-Index Metamaterial Superlens," *Applied Physics Letters*, **90**, 254102 (2007).

[33] S. K. Ghosh and T. Pal, “Interparticle Coupling Effect on the Surface Plasmon Resonance of Gold Nanoparticles: From Theory to Applications," *Chemical Reviews*, **107**, 4797–4862 (2007).

[34] S. Szunerits and R. Boukherroub, “Sensing Using Localised Surface Plasmon Resonance Sensors," *Chemical Communications*, **48**, 8999–9010 (2012).

[35] Y. Shi, J. Wang, C. Wang, T.-T. Zhai, W.-J. Bao, J.-J. Xu, X.-H. Xia and H.-Y. Chen, “Hot Electron of Au Nanorods Activates the Electrocatalysis of Hydrogen Evolution on MoS2 Nanosheets," *Journal of the American Chemical Society*, **137**, 7365–7370 (2015).

[36] N. K. Pathak, Parthasarathi, G. K. Pandey and R. Sharma. A Perspective on Plasmonics within and beyond the Electrostatic Approximation. *Plasmonics*. IntechOpen, 2018.

[37] E. Ringe, M. R. Langille, K. Sohn, J. Zhang, J. Huang, C. A. Mirkin, R. P. Van Duyne and L. D. Marks, “Plasmon Length: A Universal Parameter to Describe Size Effects in Gold Nanoparticles," *The Journal of Physical Chemistry Letters*, **3**, 1479–1483 (2012).

[38] V. Myroshnychenko, J. Rodríguez-Fernández, I. Pastoriza-Santos, A. M. Funston, C. Novo, P. Mulvaney, L. M. Liz-Marzán and F. J. García de Abajo, “Modelling the Optical Response of Gold Nanoparticles," *Chemical Society Reviews*, **37**, 1792–1805 (2008).

[39] E. Ringe, J. M. McMahon, K. Sohn, C. Cobley, Y. Xia, J. Huang, G. C. Schatz, L. D. Marks and R. P. Van Duyne, “Unraveling the Effects of Size, Composition, and Substrate on the Localized Surface Plasmon Resonance Frequencies of Gold and Silver Nanocubes: A Systematic Single-Particle Approach," *Journal of Physical Chemistry C*, **114**, 12511–12516 (2010).

[40] S. A. Maier. *Plasmonics: Fundamentals and Applications*. USA: Springer, 2007.

[41] F. Wang and Y. R. Shen, “General Properties of Local Plasmons in Metal Nanostructures," *Physical Review Letters*, **97**, 206806 (2006).

[42] R. Guo, T. K. Hakala and P. Törmä, “Geometry Dependence of Surface Lattice Resonances in Plasmonic Nanoparticle Arrays," *Physical Review B*, **95**, 155423 (2017).

[43] V. E. Babicheva and A. B. Evlyukhin, “Metasurfaces with Electric Quadrupole and Magnetic Dipole Resonant Coupling," *ACS photonics*, **5**, 2022–2033 (2018).

[44] B. García-Cámara, F. Moreno, F. González and O. J. F. Martin, “Light Scattering by an Array of Electric and Magnetic Nanoparticles," *Optics Express*, **18**, 10001–10015 (2010).

[45] A. Muravitskaya, A. Movsesyan, S. Kostcheev and P.-M. Adam, “Polarization Switching between Parallel and Orthogonal Collective Resonances in Arrays of Metal Nanoparticles," *Journal of the Optical Society of America B*, **36**, E65–E70 (2019).

[46] V. Giannini, Y. Francescato, H. Amrania, C. C. Phillips and S. A. Maier, “Fano Resonances in Nanoscale Plasmonic Systems: A Parameter-Free Modeling Approach," *Nano Letters*, **11**, 2835–2840 (2011).

[47] V. L. Loke, M. Pinar Mengüç and T. A. Nieminen, “Discrete-Dipole Approximation with Surface Interaction: Computational Toolbox for MATLAB," *Journal of Quantitative Spectroscopy and Radiative Transfer*, **112**, 1711–1725 (2011).

[48] E. M. Purcell and C. R. Pennypacker, “Scattering and Absorption of Light by Nonspherical Dielectric Grains," *Astrophysical Journal*, **186**, 705–714 (1973).

[49] M. J. Huttunen, K. Dolgaleva, P. Törmä and R. W. Boyd, “Ultra-Strong Polarization Dependence of Surface Lattice Resonances with Out-of-Plane Plasmon Oscillations," *Optics Express*, **24**, 28279–28289 (2016).

[50] S. Aghili, A. Amini, L. S. Dizaj and K. Dolgaleva, “THz Plasmonic Metasurface Based on a Periodic Array of InSb Metamolecules with Narrow Resonances," *Optics Communications*, **508**, 127805 (2022).

[51] T. Jensen, L. Kelly, A. Lazarides and G. C. Schatz, “Electrodynamics of Noble Metal Nanoparticles and Nanoparticle Clusters," *Journal of Cluster Science*, **10**, 295–317 (1999).

[52] B. T. Draine, “The Discrete-Dipole Approximation and Its Application to Interstellar Graphite Grains," *Astrophysical Journal*, **333**, 848–872 (1988).

[53] F. Capolino, D. Wilton and W. Johnson, “Efficient Computation of the 3D Green’s Function for the Helmholtz Operator for a Linear Array of Point Sources Using the Ewald Method," *Journal of Computational Physics*, **223**, 250–261 (2007).

[54] D. Sullivan. *Electromagnetic Simulation Using the FDTD Method*. Wiley, 2013.

[55] E. Garmire, “Nonlinear Optics in Daily Life," *Optics Express*, **21**, 30532–30544 (2013).

[56] A. Cinal, A. Demirok, T. Yasar, A. Yazicioglu, H. I. Yener and A. Kiliç, “Nd:YAG Laser Posterior Capsulotomy after Pediatric and Adult Cataract Surgery," *Annals of Ophthalmology*, **39**, 321–326 (2007).

[57] Z. Hou, L. Wang, M. Xia, D. Yan, Q. Zhang, L. Zhang, L. Liu, D. Xu, D. Zhang, X. Wang, R. Li and C. Chen, “Stable, High Power, High Efficiency Picosecond Ultraviolet Generation at 355 nm in K3B6O10Br Crystal," *Optics Communications*, **416**, 71–76 (2018).

[58] D. Karnakis, A. Kearsley and M. Knowles, “Ultrafast Laser Patterning of OLEDs on Flexible Substrate for Solid-State Lighting," *Journal of Laser Micro/Nanoengineering*, **4**, 218–223 (2009).

[59] S. Liu, P. P. Vabishchevich, A. Vaskin, J. L. Reno, G. A. Keeler, M. B. Sinclair, I. Staude and I. Brener, “An All-Dielectric Metasurface as a Broadband Optical Frequency Mixer," *Nature Communications*, **9**, 2507–2513 (2018).

[60] S. Roke, M. Bonn, A. Petukhov, C. en grenslagen, Physical, C. C. 1 and D. Scheikunde, “Nonlinear Optical Scattering: The Concept of Effective Susceptibility," *Physical Review B*, **70**, 115106 (2004).

[61] K. O’Brien, H. Suchowski, J. Rho, A. Salandrino, B. Kante, X. Yin and X. Zhang, “Predicting Nonlinear Properties of Metamaterials from the Linear Response," *Nature Materials*, **14**, 379–383 (2015).

[62] A. Krasnok, M. Tymchenko and A. Alu, “Nonlinear Metasurfaces: A Paradigm Shift in Nonlinear Optics," *Materials Today*, **21**, 8–21 (2018).

[63] F. Wang, A. B. F. Martinson and H. Harutyunyan, “Efficient Nonlinear Metasurface Based on Nonplanar Plasmonic Nanocavities," *ACS Photonics*, **4**, 1188–1194 (2017).

[64] T. Wu, Y. Luo, S. A. Maier and L. Wei, “Phase-matching and Peak Nonlinearity Enhanced Third-Harmonic Generation in Graphene Plasmonic Coupler," *Physical Review Applied*, **11**, 014049 (2019).

[65] A. Noor, A. R. Damodaran, I.-H. Lee, S. A. Maier, S.-H. Oh and C. Ciracì, “Mode-Matching Enhancement of Second-Harmonic Generation with Plasmonic Nanopatch Antennas," *ACS Photonics*, **7**, 3333–3340 (2020).

[66] M. Celebrano, X. Wu, M. Baselli, S. Grossmann, P. Biagioni, A. Locatelli, C. De Angelis, G. Cerullo, R. Osellame, B. Hecht, L. Duò, F. Ciccacci and M. Finazzi, “Mode Matching in Multiresonant Plasmonic Nanoantennas for Enhanced Second Harmonic Generation," *Nature Nanotechnology*, **10**, 412–417 (2015).

[67] M. J. Huttunen, O. Reshef, T. Stolt, K. Dolgaleva, R. W. Boyd and M. Kauranen, “Efficient Nonlinear Metasurfaces by Using Multiresonant High-Q Plasmonic Arrays," *Journal of the Optical Society of America B*, **36**, E30–E35 (2019).

[68] M. J. Huttunen, P. Rasekh, R. W. Boyd and K. Dolgaleva, “Using Surface Lattice Resonances to Engineer Nonlinear Optical Processes in Metal Nanoparticle Arrays," *Physical Review A*, **97**, 053817 (2018).

[69] T. Stolt, A. Vesala, H. Rekola, P. Karvinen, T. K. Hakala and M. J. Huttunen, “Multiply-Resonant Second-Harmonic Generation Using Surface Lattice Resonances in Aluminum Metasurfaces," *Optics Express*, **30**, 3620–3631 (2022).

[70] R. Czaplicki, J. Mäkitalo, R. Siikanen, H. Husu, J. Lehtolahti, M. Kuittinen and M. Kauranen, “Second-Harmonic Generation from Metal Nanoparticles: Resonance Enhancement versus Particle Geometry," *Nano Letters*, **15**, 530–534 (2015).

[71] B. Auguié and W. L. Barnes, “Collective Resonances in Gold Nanoparticle Arrays," *Physical Review Letters*, **101**, 143902 (2008).

[72] D. Gérard and S. K. Gray, “Aluminium Plasmonics," *Journal of Physics D: Applied Physics*, **48**, 184001 (2014).

[73] C. Langhammer, M. Schwind, B. Kasemo and I. Zori, “Localized Surface Plasmon Resonances in Aluminum Nanodisks," *Nano Letters*, **8**, 1461–1471 (2008).

[74] M. W. Knight, N. S. King, L. Liu, H. O. Everitt, P. Nordlander and N. J. Halas, “Aluminum for Plasmonics," *ACS Nano*, **8**, 834–840 (2014).

[75] M. Castro-Lopez, D. Brinks, R. Sapienza and N. F. van Hulst, “Aluminum for Nonlinear Plasmonics: Resonance-Driven Polarized Luminescence of Al, Ag, and Au Nanoantennas," *Nano Letters*, **11**, 4674–4678 (2011).

[76] O. Svelto. *Principles of Lasers*. New York, NY: Springer US, 2010.

[77] Y. Nishijima, L. Rosa and S. Juodkazis, “Surface Plasmon Resonances in Periodic and Random Patterns of Gold Nano-Disks for Broadband Light Harvesting," *Optics Express*, **20**, 11466–11477 (2012).

[78] J. Martin and J. Plain, “Fabrication of Aluminium Nanostructures for Plasmonics," *Journal of Physics D: Applied Physics*, **48**, 184002 (2015).

[79] D. Khlopin, F. Laux, W. P. Wardley, J. Martin, G. A. Wurtz, J. Plain, N. Bonod, A. V. Zayats, W. Dickson and D. Gérard, “Lattice Modes and Plasmonic Linewidth Engineering in Gold and Aluminum Nanoparticle Arrays," *Journal of the Optical Society of America B*, **34**, 691–700 (2017).

[80] T. Harimoto, B. Yo and K. Uchida, “A Novel Multipass Scheme for Enhancement of Second Harmonic Generation," *Optics Express*, **19**, 22692–22697 (2011).

[81] G. Albrecht, S. Kaiser, H. Giessen and M. Hentschel, “Refractory Plasmonics without Refractory Materials," *Nano Letters*, **17**, 6402–6408 (2017).

[82] T. Stolt and M. J. Huttunen, “Broadband Frequency Conversion of Ultrashort Pulses Using High-Q Metasurface Resonators," *New Journal of Physics*, **24**, 025004 (2022).

[83] J. F. Algorri, D. C. Zografopoulos, A. Ferraro, B. García-Cámara, R. Beccherelli and J. M. Sánchez-Pena, “Ultrahigh-Quality Factor Resonant Dielectric Metasurfaces Based on Hollow Nanocuboids," *Optics Express*, **27**, 6320–6330 (2019).

[84] Y. Kivshar, “All-Dielectric Meta-Optics and Non-Linear Nanophotonics," *National Science Review*, **5**, 144–158 (2018).

APPENDIX A: SPECTRAL LOCATION OF LOCALIZED SURFACE PLASMON RESONANCES

In order to estimate the location of a single-particle LSPR for our metasurfaces, we fabricated a new sample with randomly arranged V-shaped aluminum nanoparticles placed on a dielectric substrate. The randomness guarantees that the particles don't exhibit long-range order and eliminates the possibility of coherent grating interference. To strengthen the extinction spectra, we increased the particle density so that the sample possesses a particle density similar to 300 $\times$ 300 nm^2 square array. Figure A.1 shows the transmission versus the wavelength at normal incidence for the randomly patterned array.

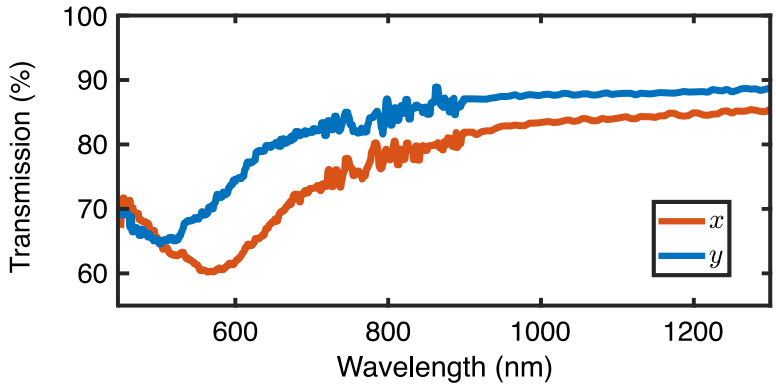

Figure A.1. When arranged on a random lattice, the metasurface exhibits only single-particle LSPRs. For our samples, they occur at 550 nm and 475 nm for x- (red) and y-polarized light.

The transmission spectra reveal a visible peak at the LSPR with a linewidth of approximately 100 nm. For x-polarized light, the SLR occurs at 550 nm, while for y-polarized light the SLR occurs at 475 nm.